




5-2022

Development of Arduino-based portable systems for electroanalytical detection

Jiamei Huang

Electrical Engineering and Computer Science, UTK, jhuang37@vols.utk.edu

Follow this and additional works at: https://trace.tennessee.edu/utk_gradthes

 Part of the [Electrical and Electronics Commons](#)

Recommended Citation

Huang, Jiamei, "Development of Arduino-based portable systems for electroanalytical detection. " Master's Thesis, University of Tennessee, 2022.
https://trace.tennessee.edu/utk_gradthes/6421

This Thesis is brought to you for free and open access by the Graduate School at TRACE: Tennessee Research and Creative Exchange. It has been accepted for inclusion in Masters Theses by an authorized administrator of TRACE: Tennessee Research and Creative Exchange. For more information, please contact trace@utk.edu.

To the Graduate Council:

I am submitting herewith a thesis written by Jiamei Huang entitled "Development of Arduino-based portable systems for electroanalytical detection." I have examined the final electronic copy of this thesis for form and content and recommend that it be accepted in partial fulfillment of the requirements for the degree of Master of Science, with a major in Electrical Engineering.

Jie Wu, Major Professor

We have read this thesis and recommend its acceptance:

Jie Wu, Gong Gu, Qing Cao

Accepted for the Council:

Dixie L. Thompson

Vice Provost and Dean of the Graduate School

(Original signatures are on file with official student records.)

**Development of Arduino-based portable systems for electroanalytical
detection**

A Thesis Presented for the
Master of Science
Degree
The University of Tennessee, Knoxville

Jiamei Huang
May 2022

Copyright © 2022 by Jiamei Huang
All rights reserved.

ABSTRACT

This work presents the development of a multi-mode electroanalytical detection system based on Arduino microcontroller board. First, a multichannel impedance readout system is designed for alternating current electrokinetics (ACEK) based capacitive sensing. ACEK phenomena on 100 μ m interdigitated electrodes are observed via fluorescent particles as well as bioparticles, which illustrate the mechanisms of ACEK target enrichment for the capacitive sensing method. I2C multiplexer is applied to allow multiple impedance converters to work together providing continuous AC signals for ACEK capacitive sensing. Second, an electronic nose composed of three modules including a gas sensor array, a circuit for signal acquisition integrated with Arduino microcontroller board, and a PC for signal analysis is designed. A backpropagation neural network with one hidden layer and one output layer is trained to classify gas samples from binary and ternary mixtures of acetone, ethanol, and isopropyl alcohol. Three features are extracted from transient signals in a short time (as compared to steady-state signals), and the classification is done within 1 minute after gas reached the surface of the sensors. Third, a low-cost portable potentiometric sensing system for the detection of heavy metals in water is developed and assessed by testing with hand-fabricated all-solid-state Pb^{2+} and Cd^{2+} ion-selective electrodes (ISEs). To avoid the use of a multimeter, an extended-gate metal-oxide-semiconductor field-effect transistor (MOSFET) is applied to the readout circuit and integrated with an Arduino microcontroller board. ALD1106 matched MOSFET pair is chosen for differential sensing to overcome the possible drift problem of ISEs. With a threshold voltage of 0.7 V while operating at the subthreshold region, the MOSFET could be biased via a potentiometer to avoid the use of a voltage source. Last, the three different analytical detections are integrated into one multi-mode system in the design.

TABLE OF CONTENTS

Chapter 1	Introduction.....	1
1.1	Research background.....	1
1.2	Types of electroanalytical sensors	3
1.2.1	Impedance readout- biofluid based electrode sensors.....	3
1.2.2	Potentiometric sensors	4
1.2.3	Metal oxide semiconductor sensors	5
1.3	Scope and Research Goal	6
1.4	Contribution	7
Chapter 2	Sensing mechanism and sensor array	8
2.1	ACEK biosensing theory	8
2.1.1	Interfacial capacitive sensing	8
2.1.2	ACEK mechanisms	9
2.1.3	ACEK observations	10
2.2	Sensor array	12
2.2.1	ACEK biosensor array	12
2.2.2	MOS gas sensor array	12
Chapter 3	Microcontroller based readout system design.....	13
3.1	AD5933 based ACEK capacitive sensing system	13
3.1.1	AD5933 impedance converter	13
3.1.2	Low voltage measurement design.....	14
3.1.3	Peripherals.....	15
3.1.4	Multichannel	15
3.1.5	Power module	16
3.1.6	PCB design of the system	17
3.1.7	Coding.....	17
3.1.8	Sequenced measurement	19
3.2	Potential based detection system	19

3.2.1 Circuits	20
3.2.2 Laboratory setup	20
3.2.3 Selection of gas sensors	21
3.2.4 Sample acquisition	23
3.2.5 Extended-Gate FET readout circuit for Potentiometric sensing	23
3.3 Integration of multi-mode sensing	25
Chapter 4 Measurements and detection results	26
4.1 ACEK measurements	26
4.1.1 System calibration test	26
4.1.2 Impedance measurement	26
4.2 VOC gas measurements	27
4.2.1 Feature extraction and selection	27
4.2.2 Classification algorithms and results	28
4.2.3 Regression algorithms and results	29
Chapter 5 Conclusions	31
References	32
Appendix	39
Vita	65

LIST OF TABLES

Table A- 1. Gas sensors in the array	63
Table A- 2. Correlation coefficient between sensors.....	63
Table A- 3. Principal component analysis of the sensor array.	64

LIST OF FIGURES

Figure A- 1. (a) a simple IDE design, (b) 200 μm width/gap hand-made IDE, (c) 2 μm width/gap SAW resonator.....	40
Figure A- 2. Schematic of biofluid-based DNAzyme sensor: (a) Impedance readout of the IDE sensor, (b) DNAzyme on IDE introduced by biofluid, (c) Substrate and DNAzyme sequences. (from published prior work [7])	40
Figure A- 3. Schematic of coated-wire all-solid-state ISE and reference electrode in reference [27].	41
Figure A- 4. Hand-made all-solid-state Pb^{2+} ISE sensor	41
Figure A- 5. Basic measuring circuit of (a) MQ series (b) TGS series gas sensors (from datasheet)	42
Figure A- 6. Equivalent circuit for IDE biosensor.....	42
Figure A- 7. Schematic of interfacial capacitance changes at different stages, (a) before probe immobilization, (b) after probe immobilization and blocking, (c) after target binding with probe.(from published prior work [31])	42
Figure A- 8. Image series show DEP force on yeast cells at 100 kHz in DI water	43
Figure A- 9. Image series show 1.0 μm fluorescent particle ACET movement at 10 kHz 0.5 \times SSC	43
Figure A- 10. ACEO vortices shown by fluorescent particles at 100 kHz 0.1 \times PBS.....	43
Figure A- 11. Image series showing particle movements with ACEO vortices at 10 kHz 0.1 \times PBS	44
Figure A- 12. Image series showing combination of DEP and ACEO at 1 kHz in DI water	45
Figure A- 13. Image series showing how yeast cells move on electrode	45
Figure A- 14. (a) Top (b) bottom view of the IDE sensor array	45
Figure A- 15. MOS gas sensor array	46
Figure A- 16. Bioimpedance measuring method. (A) Model of measurement, (B)Architecture of gain-phase detector (from published prior work [35]).....	46

Figure A- 17. Block overview of AD5933 (from datasheet [37])	47
Figure A- 18. Capacitive sensing circuit.....	47
Figure A- 19. Schematic of the low voltage capacitive sensing circuit.....	48
Figure A- 20. Schematic of the I2C multiplex module.....	48
Figure A- 21 Schematic design of the power module.....	49
Figure A- 22. Layout of the multichannel impedance measurement system.....	50
Figure A- 23. 3D layout of the multichannel impedance measurement system	50
Figure A- 24. Flowchart of the ACEK biosensing system	51
Figure A- 25. Oscilloscope screenshot of the sequenced measurement (a) frame 215 (b) frame 216	52
Figure A- 26. Schematic of the microcontroller-based signal acquisition system	53
Figure A- 27 Scheme of the gas detection experimental system	53
Figure A- 28 (a) Responses of the 6 MOS sensors toward acetone; (b) Single and mixed gas response curve of TGS2602. The sampling rate is 10 Hz, i.e. the x-axis is from 0 to 50 s.....	54
Figure A- 29 Response curve of the 6 MOS sensors to different VOCs: 2 ml of 8.3% acetone (in air); 10 ml of 1.71% IPA (in air); 10 ml of 1.74% ethanol (in air). The sampling rate is 10 Hz, i.e. the x-axis is from 0 to 50 s.....	54
Figure A- 30. Schematic of the Extended-gate FET circuit.....	55
Figure A- 31. Experimental setup of the potentiometric sensing system	55
Figure A- 32. ALD1106 transfer curve.....	56
Figure A- 33. Screenshot of the MATLAB & Arduino Serial Communication.....	56
Figure A- 34. Potentiometric sensing result	57
Figure A- 35. Schematic of the multi-mode sensing system	57
Figure A- 36. Calibration test with 1200 Ω resistor	58
Figure A- 37. Impedance reading of 2700pF capacitor at 100kHz.....	58
Figure A- 38. Photo of the ACEK impedance readout system.....	59
Figure A- 39. Impedance readings when calibrated with the 1200 Ω resistor. Error bar shows the standard deviation.	59

Figure A- 40 (a) Response curve and parameters in phase space; Response curve to different amounts of ethanol and acetone in phase space, (b) TGS2602, (c) MQ136 (Solid line represents ethanol, dotted line represents acetone) 60

Figure A- 41. Diagram of the neural network..... 61

Figure A- 42. Confusion matrix of classification results 61

Figure A- 43. Target versus predicted amount of gas in VOC mixture (a) Multivariate linear regression (b) BPNN..... 62

CHAPTER 1

INTRODUCTION

1.1 Research background

The development of low-cost, versatile, and portable data acquisition and processing systems for electroanalytical detection is of great importance. For the past decade, a large number of microcontroller based potentiostat for electrochemical detections are designed by researchers [1] [2] [3] [4]. However, most of these systems are designed for biosensors or chemical sensors in a particular application. Moreover, for the application of portable potentiometric electronic tongue, where small voltage differences are to be measured, a benchtop multimeter with high input impedance is usually required, which makes the whole system not portable [5].

Alternating current electrokinetics (ACEK) capacitive sensing technology has shown high potential in the detection of bacteria [6], heavy metals [7] as well as small molecules [8]. This sensing method uses interdigitated microelectrodes (IDEs) as a basic sensor structure, combining affinity biosensing technology with ACEK target enrichment technology. It measures the capacitance changes of the IDE sensor under AC voltage with a selected amplitude and frequency, and uses the capacitance change rate (dC/dt) in a time period of 15~30s as the test result. A palm-size analyzer for ACEK capacitive sensing is designed by Liu [9] in 2017. This device is a single channel sensing system and is not able to test with multiple channels. As a continuation of Liu's work, Queslati designed a multiplexed ACEK sensing system in 2019 [10]. Instead of using an I2C multiplexer to allow multiple impedance converters to work synchronously, her work uses a CMOS analog multiplexer (ADG1604) to switch between the sensors to realize time-division multiplexing. With one impedance converter, which contains only one signal generator, the measurement for different channels in this system is either done sequentially one by one or via time division. The former method is time-consuming especially when more

channels are involved, and the latter one will weaken ACEK effects on each channel while introducing more noise.

While capacitive sensing works well with affinity-based biodetection, many biochemical sensors are based on amperometric methods, such as potentiometric sensors, which are good candidates to integrate into a multiplexed sensing system. Potentiometric ion-selective sensors are of great importance in applications of in situ monitoring of aquatic systems. Ion-selective sensors have exhibited excellent analytical performances for pH tests as well as the detection of trace heavy metals (e.g., Pb^{2+} , Cd^{2+}) in water [11]. Conventional ion-selective electrodes (ISEs) are composed of an ion-selective membrane, an inner filling solution, and a reference electrode connecting to the potentiometer [12]. Since the invention of coated wire electrodes in the 1970s, all-solid-state ISEs have received much attention from researchers due to the easy miniaturization when compared with conventional liquid contact ISEs. Similar to an electronic nose, an array of potentiometric sensors combined with a pattern recognition algorithm could form an electronic tongue.

In addition to biodetection, gas phase detection of chemicals also helps to identify potential hazards. Detection of poisonous or explosive gases emit from industry productions and indoor environments is important for environmental protection as well as human health. Volatile organic compounds (VOCs) include a variety of chemicals that can be found in both indoor and outdoor air. Building materials, home & personal care products, combustion processes (e.g., paint, pressed wood products, cleaners, smoking, cooking) are the most common indoor VOCs sources. Major outdoor sources include traffic emissions, wood burning, oil & gas extraction, and industrial emissions. According to EPA, some of the VOCs may have short- and long-term adverse health effects such as irritation and headaches, damage to organs, or cause cancer [13]. Currently, there is a wide range of commercially available gas sensors for various applications. Based on the type of the sensing element, gas sensors are typically classified into the following types: metal oxide semiconductor (MOS) type [14], catalytic (or calorimetric) type [15], electrochemical type [16], infrared type [17], capacitive type [18], and surface acoustic wave (SAW) type [19].

Among these types of sensors, MOS-based sensors are the most studied group of gas sensors with increasing popularity for gas sensing, especially for VOC detection. However, the selectivity of MOS gas sensors is poor due to the well-known cross-sensitivity in MOS gas sensors. As a result, no MOS gas sensor is selective to a single gas, and a single MOS gas sensor is not adequate for specific recognition when challenged with a gas mixture [20]. The selectivity problem of MOS gas sensors could be alleviated by using an array of sensors with different sensitivities along with a pattern recognition algorithm. Each sensor in the array has a preferred “target” gas that would yield a higher response than other gas species. A sensor array with pattern recognition algorithm is widely adopted in gas identification systems and is commonly known as an electronic nose [21] [22].

A portable electroanalytical detection system based on a microcontroller can avoid the use of bulky and expensive lab equipment like potentiostat, multimeter, and DC voltage source. The motivation for integrating the ACEK capacitive sensing module, electronic nose, and electronic tongue into the multimode system is to reduce cost while implementing different detections simultaneously.

1.2 Types of electroanalytical sensors

Owing to the development of affordable, user-friendly, and portable analytical tools, electroanalytical sensing technology is growing rapidly nowadays. This section reviews the three types of electroanalytical sensors that are adopted by the Arduino microcontroller based detection system.

1.2.1 Impedance readout- biofluid based electrode sensors

Interdigitated electrode (IDE) consists of an array of interwoven electrodes on a substrate that are generally used to measure impedance. It has gained considerable interest in recent years as electrical transducers for biosensing [8] [23] [24]. The absence of reference electrodes and ease of miniaturization are two main advantages of IDE sensors. Figure A-1 shows the IDE sensors. All tables and figures are located in the appendix. Figure A-1 (a) is a simple design of IDE, (b) is a hand-made 400 μm width/gap IDE with FR4 substrate,

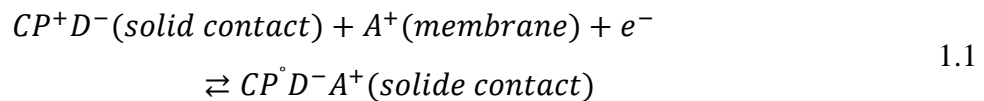
and (c) is a commercial SAW resonator which contains 2 μm width/gap IDE on a ceramic substrate.

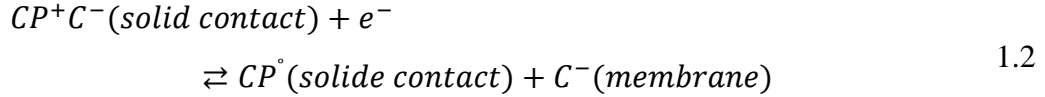
In a previous work [7], a gold-plated IDE of 100μm width/gap IDE is used as a sensor for sensitive and rapid detection of Pb²⁺ ions. Figure A- 2 shows the schematic of our sensor with DNA strands involved on the gold surface of IDE, and impedance measurements by a single-channel commercial impedance analyzer.

1.2.2 Potentiometric sensors

Potentiometric sensing measures the potential difference between two electrodes (generally ion-selective electrodes (ISEs) and reference electrodes in liquid phase) when no current is present. The electrical potential of the ISEs could be used to determine the analytical quantity of some components. The reference electrode is to provide a defined reference potential in the measurement. [25] [26] Conventional ISEs contain inner filling solutions which serve as liquid contacts to separate the sensing membrane from the inner reference element. This makes it sensitive to changes in temperature and pressure as well as the evaporation of the inner filling solutions. Moreover, the miniaturization of liquid contact ISEs is limited by the use of inner liquid, making it hard to meet the requirements for low-cost portable devices with easy maintenance and simple operation. [27] Different from conventional ISEs, all-solid-state ISEs use solid contact as the ion-to-electron transducer. As shown in Figure A- 3 [27], an all-solid-state electrode contains a thin layer of membrane (ion-selective or reference membrane), a coated wire (connecting lead), and a solid contact between membrane and wire (ion-to-electron transducer).

Conducting polymers are effective ion-to-electron transducers while serving as solid contact for an all-solid-state ISE. The potential difference across the ion-selective membrane and the solid contact, conducting polymer, is determined by analyte ion distribution. Whereas the interfacial potential between conducting polymer and the substrate (coated wire) is by the redox reactions in the following equations:





in which CP refers to conducting polymer, A^+ represent the analyte ion (target ion of a detection), D^- and C^- are the doping and hydrophobic counter ion added to the conducting polymer. Conducting polymer serves as a redox buffer transferring ions to electrons while being oxidized or reduced.

Figure A- 4 shows a hand-made all-solid-state ISE sensor with Pb^{2+} ion-selective membrane. Similar to the hand-made IDE sensors in Figure A- 1 (b), the base structure of the ISE sensor in this work is also fabricated by PCB etching. Nickel and gold layers are plated to the electrode sequentially. Poly (3,4-ethylenedioxythiophene) (PEDOT), which serves as solid contact layer, is coated on the gold electrode surface by electrochemical deposition. Then a thin layer of Pb^{2+} selective membrane is coated by spin coating. Finally, the edges of the sensing membrane as well as the rest of the electrode is sealed by epoxy.

1.2.3 Metal oxide semiconductor sensors

MOS gas sensors are the most investigated group of gas sensors. Because the response and recovery times decrease with temperature, it usually needs to work at high temperatures. MOSs can be divided into two groups according to the operating temperature: (1) surface conductance materials (e.g. ZnO, SnO₂) operating at 400°C-600°C and (2) bulk conductance materials (e.g. TiO₂, CeO₂) operating at >700°C [14]. The required preheating time of MOS sensor is usually more than 24 hours.

When metal oxide semiconductor particles (e.g. tin dioxide) are heated in clean air, donor electrons in the metal oxide are attached to oxygen adsorbed on the particle surface. The lack of free electrons reduces electric current flow. In the presence of target VOCs, the MOS sensor reacts with the VOCs. The electrons once attached to the oxygen molecules are released into the metal oxide, increasing the current flow and decreasing the sensor resistance. The sensor resistance decreases correspondingly, thus realizing the detection of VOCs in the air [28].

Figure A- 5 shows the basic measuring circuit of MOS sensors from two major manufacturers: (a) HANWEI® MQ series and (b) Figaro® TGS series gas sensors. The packaged sensors operate at room temperature. However, a 5 V DC heater voltage is needed for the inside sensing element to maintain a working temperature at 400°C. When the reaction of specific gases with the sensing elements leads to a change in the sensor resistance R_s , changes in voltage could be obtained via the circuit shown in Figure A- 5. By choosing an appropriate value for the load resistor R_L , voltage levels at V_{OUT} could indicate the presence and the level of target gases.

1.3 Scope and Research Goal

The development of portable analytical devices for on-site electroanalytical detection is relatively straightforward. However, one of the unsettling issues for some electroanalytical sensors is the selectivity of the sensor. While the sensor is sensitive to the target, it also responds to non-target interferences. To overcome the selectivity problem, an array of sensors with different sensitivities is usually used. Hence, multichannel measurement is preferred.

Affinity biosensors usually take a long time to yield results. By introducing alternating current electrokinetic (ACEK) effects for target enrichment, the testing time required for one single capacitive sensing sensor could be shortened to 15 seconds. However, the waiting period is still too long when multiple samples are to test. To further accelerate the testing process, multiplexed impedance readout system for multi-channel ACEK capacitive sensing as well as a multi-channel sensor array are designed in this work. Moreover, a multi-mode detection system that integrates ACEK capacitive sensing technique with potential based sensing is designed in this work.

1.4 Contribution

This work designed three different electroanalytical detection systems based on Arduino microcontroller boards: the impedance readout system for ACEK capacitive sensing, the electronic nose system, and the extended-gate FET potentiometric sensor readout system.

ACEK phenomena on 100 μ m interdigitated electrodes are observed via fluorescent particles as well as bioparticles, which illustrate the mechanisms of ACEK target enrichment for the capacitive sensing method. Then multiplexed testing is realized in the design of the impedance readout system for ACEK capacitive sensing.

An electronic nose system aims to detect volatile organic compounds (VOC) in indoor ventilation system is designed. Correlation coefficient and principal component analysis are used while selecting gas sensors for the sensing array. A classifier and a regression model based on backpropagation neural network are used for qualitative and quantitative detection of VOC mixtures. The test accuracy of the classification on acetone, ethanol, isopropyl alcohol gas as well as its binary and ternary gas mixtures is 82.6%.

To expand the function of the Arduino microcontroller board based electroanalytical detection system, an extended-gate FET readout system for potentiometric sensing is designed, in which small voltage differences generated by all-solid-state ion-selective electrodes are amplified by the FET before being measured by analog input pins of the microcontroller.

CHAPTER 2

SENSING MECHANISM AND SENSOR ARRAY

2.1 ACEK biosensing theory

The use of electrokinetics in microfluidic systems is common. It usually serves two purposes. The one is for fluid pumping, which transports a range of different species from biomolecules to cells; The other is for particle manipulation, which usually means concentrating or separating particles for analysis. Direct current electrokinetics (DCEK) need a high voltage level to generate electrokinetic flow, which may cause electrochemical reactions and generate bubbles when gas is produced. On the other hand, the induced charges from alternative current electrokinetics (ACEK) change polarity with the external electric field, preventing reactions even at a relatively high voltage level. Thus, ACEK has higher transport efficiency when compared with DCEK.

2.1.1 Interfacial capacitive sensing

Capacitive sensing is a technology that detects or measures something conductive based on the capacitive coupling theory [29]. Interfacial capacitance is a function of electric double layer capacitance [30]. When IDE is immersed in electrolytic solutions, an electric double layer will form between the aqueous solution and the interface of the electrodes. Determined by the electronic structure of the IDE introduced in section 1.2.1, the electrode cell can be represented by the equivalent circuit in Figure A- 6:

Solution resistance of the sensor is represented by R_{sol} and the interfacial capacitance is modeled by a constant phase element CPE_{int} and a resistive path R_{leak} . The changes in the electronic element values reflect the changes happen on the sensor surface during sensor preparation or detection. Use our DNA sensor in [31] (Figure A- 7) as an example, the surface area of the IDE sensor, which is one of the key factors in capacitance calculation, varies in different stages of probe immobilization and target binding. Represent

by A_0 , A_{b0} and A_b , the surface area in relation to interfacial capacitance increases in the DNA probe immobilization and target miRNA binding process.

2.1.2 ACEK mechanisms

Interfacial capacitive sensing depends on the changes in capacitance due to the probe & target binding above the surface of the microelectrodes. This process can be accelerated and enhanced by ACEK phenomenon. ACEK mainly includes dielectrophoresis (DEP), AC electro-osmosis (ACEO), and AC electrothermal effect (ACET) [32].

- Dielectrophoresis

DEP explained the phenomenon of how a force is exerted on a dielectric particle when the particle is subjected to a non-uniform electric field [33]. The electric field polarizes the particle and exerts a force on it to move it. The velocity can be described by the following equation:

$$\langle u_{DEP} \rangle = \frac{a^2 \varepsilon_m}{6\eta} \text{Re} \left[\frac{\tilde{\varepsilon}_p - \tilde{\varepsilon}_m}{\tilde{\varepsilon}_p + 2\tilde{\varepsilon}_m} \right] \nabla |E|^2 \quad 2.1$$

where a is the diameter of the particle; $\tilde{\varepsilon}_p$ and $\tilde{\varepsilon}_m$ are complex permittivity of the particle and the suspending medium; η is viscosity of the medium. We can see from equation 2.1 that DEP velocity of a particle can be positive or negative determined by the sign of $\tilde{\varepsilon}_p - \tilde{\varepsilon}_m$, which depends on the frequency.

- AC electro-osmosis

ACEO is a phenomenon of induced-charge electro-osmosis flow around electrodes when AC voltage is applied [34]. Firstly, the electrodes are become capacitively charged by AC voltage signal. Then counter-ions accumulated at the surfaces of the charged electrodes. When the counter-ions migrate with/against electric field, which is tangential to the electrode surface, it generates fluid motion due to fluid viscosity [32]. The basic scaling of ACEO flow is given by [34]

$$\langle \mathbf{u} \rangle \propto \frac{\varepsilon V^2}{\eta(1+\delta)L \left[\frac{\omega}{\omega_c} + \frac{\omega_c}{\omega} \right]^2} \quad 2.2$$

$$\omega_c \propto \frac{D(1+\delta)}{\lambda L} \quad 2.3$$

where V is the applied AC voltage; ε is the permittivity of the liquid; η is viscosity of the fluid; δ is the ratio of the capacitances (diffuse layer to compact layer); L is the center-to-center electrode spacing; λ is the Debye screening length; D is a characteristic ionic diffusivity. According to the equations, when $\omega = \omega_c$, ACEO flow reaches its peak velocity. That means ACEO flow weakens when the frequency of the AC voltage is too high or too low compared with the peak frequency.

- AC electrothermal effect

Biological applications usually involve fluids with high conductivities, for example, phosphate-buffered saline (PBS). While ACEO is limited to fluids with low conductivities, for example, DI water, ACET can actuate fluid motion in more conductive liquids.

ACET refers to fluid motion due to the interactions of AC electric fields and temperature gradients in the fluid. Joule heating of the electrolyte causes temperature gradients that yield fluid motion. The velocity of the fluid motion can be estimated by

$$u_{ACET} \cong 3 \times 10^{-3} \frac{\varepsilon V^2}{\eta} \left| \frac{\partial T}{\partial y} \right| \left| \frac{1}{\sigma} \frac{\partial \sigma}{\partial T} \right| \quad 2.4$$

where T is the temperature; σ is conductivity of the fluid; $\left| \frac{\partial T}{\partial y} \right|$ is the external thermal gradient.

2.1.3 ACEK observations

Different ACEK modes on IDE are observed through a microscope. FluoSpheres[®] carboxylate modified microspheres (1.0 μm), as well as live yeast cells (3~4 μm), are used in the observation.

Figure A- 8 (a)(b)(c) are three images extracted from a video in time sequence. Yeast cells numbered 1,2 and 3 shown in (a) are dragged to the edges of the microelectrode

in (b). After that, the cell numbered 4 in (b) is dragged to the edge in (c). This could be explained by positive DEP since DEP force is along the field lines and the electric field is strongest at the edges.

Arrows of different colors pointed out four moving particles in Figure A- 9. To illustrate the directions, each arrow starts at a fixed particle and ends at the moving particle. It is clear that all the moving particles are moving in directions from metal electrode toward the FR4 substrate gap. This experiment simulates how particles move with ACET flow (which follows the direction of thermal gradient) on IDE biosensors.

While it is easy to show ACEO movements by video, it is hard to show by images. As ACEO movements are vortices, not all particles are move in the same direction at one moment. Figure A- 10 shows the trace of fluorescent microparticles moving with ACEO flow. Vortices are observed as the particles are moving fast at 100 kHz.

Another way to show ACEO by images is to track the positions of single particles. When the frequency is lower, which is 10 kHz, ACEO movements are slower correspondingly. 8 images in the Figure A- 11 are obtained from the same video but at different times, in which (a) $t=16s$, (b) $t=22s$, (c) $t=31s$, (d) $t=37s$ show ACEO movement of one particle, (e) $t=12s$, (f) $t=20s$, (g) $t=30s$, (h) $t=38s$ show the other particle.

Quite different from Figure A- 8 in which all yeast cells are located to the edges of electrode at 100 kHz, a combination of DEP and ACEO is observed at 1 kHz in Figure A- 12. As a result, most of the stabilized cells are either lined in the center of an electrode or get fixed at the edges, while active cells are rotating with the ACEO vortices near the edges.

In another video of the yeast cell observation (shown in Figure A- 13), an active yeast cell is found to fall right in the middle of an electrode after several rotations. This is similar to the ACEO observed in reference [32]. Moreover, several cells are found moving along the centerline of the electrode (shown by a dotted line arrow), in which two of them are moving toward each other. These movements are due to the charges on the cells and the electric field, and are preferred in ACEK capacitive sensing.

2.2 Sensor array

The maximum number of electroanalytical sensors in the system to form an array is mainly determined by the detection performance of the sensor as well as the required efficiency of one detection. Besides, additional cost and power consumption to add more channels also need to be considered.

2.2.1 ACEK biosensor array

Considering the capacity of I2C multiplexer and the power consumption requirements for the system, the number of ACEK sensing channels is set to be 16. Then, the structure of the ACEK sensor array is designed according to the size and arrangement of the commercial press-to-seal silicon isolator (Millipore Sigma, GBL665208) as well as 2.54mm standard edge connector. Figure A- 14 is the top and bottom view of the 16-channel ACEK sensor.

2.2.2 MOS gas sensor array

As introduced in section 1.2.3, the sensing membrane of MOS gas sensors needs to be heated to a high temperature before use. That makes power consumption of each sensor to be relatively high. The number of sensors in an electronic nose system, especially in a portable system, is limited. Just as the price of gas sensors of different models varies, the power consumptions are also different. But overall, the MQ series gas sensors have a much higher power consumption when compared with the TGS series.

As shown in Figure A- 15, MOS gas sensors are designed to line in a row on a prototyping board as the total number of sensors is relatively small.

CHAPTER 3

MICROCONTROLLER BASED READOUT SYSTEM DESIGN

3.1 AD5933 based ACEK capacitive sensing system

According to the sensing theory introduced in Chapter 2, ACEK capacitive sensing measures the change of capacitance in a required period while AC voltage signal is present continuously not only for impedance measurement, but also for target enrichment. Unlike regular multichannel impedance measurement devices, which only need one impedance converter to do time-division multiplexing, the multichannel ACEK capacitive sensing system needs one impedance converter for each channel. AD5933 high precision impedance converter is adopted in ACEK capacitive sensing system.

3.1.1 AD5933 impedance converter

Complex impedance can be calculated by applying a sinusoidal current with constant amplitude at a known frequency between two electrodes and measuring the magnitude & phase of the output voltage [35].

As shown in Figure A- 16, Z_X is the complex bioimpedance circuit, R_S is a standard resistor. Z_X can be calculated by equation 3.1:

$$Z_X = R_S \cdot \frac{U_Z}{U_S} = R_S \cdot \frac{|U_Z| \angle \varphi_1}{|U_S| \angle \varphi_2} = R_S \cdot \frac{|U_Z|}{|U_S|} \angle \theta \quad 3.1$$

The above impedance calculation method is carried out by an I-V converter. Figure A- 17 is the block overview of AD5933. As no current is flowing into the I-V amp (connected via VIN pin), the current flowing in the RFB and $Z(\omega)$ is the same ($I_{RFB}=I_Z$), RFB serves as the standard resistor R_S in equation 3.1. In other words, the gain of the I-V amp is controlled by RFB and $Z(\omega)$.

In Figure A- 17, unknown impedance is connected directly between VOUT and VIN pins. In bio-impedance measurement, when the unknown impedance to be tested is small, the signal current flowing through the impedance increased at a fixed excitation voltage. The increased sink and source current on the output of the I-V amp may cause it to operate outside of the linear region and result in significant errors in measurements. Thus, it is necessary to add an additional external amplifier circuit to the signal path of AD5933 when measuring small impedances. [13]

Figure A- 18 shows the circuit for ACEK capacitive sensing. The 47 nF capacitor serves as a high pass filter to remove the DC bias voltage from the VOUT. The AC voltage signal is then biased by $V_{DD}/2$ by the pair of 50 k Ω resistors, R4 and R7. The voltage follower (U1A) serves as a noninverting buffer. With its low output impedance and extremely high input impedance, eliminates loading effects while still maintaining the same voltage (amplitude and frequency) at the output. [36] Instead of directly connecting the RFB and $Z_{unknown}$ to the I-V amp, an additional amplifier (U1B) is used before it. A pair of 20 k Ω resistors are used to set the gain of the I-V amp to -1. The real gain of the circuit is thus controlled by CAL and $Z_{unknown}$ placed at the added external amplifier. The use of 20 k Ω resistances in the small impedance measurement circuit protects the receive side I-V amp at a fixed excitation voltage.

As the impedance of biofluid-based electrode sensors in the frequency range of 50 kHz~100 kHz is about 1.2 k Ω , the value of the calibration resistor (CAL in the circuit) should be set similar to this value. A 1.2 k Ω resistor is chosen as CAL resistor in the capacitance sensing circuit.

3.1.2 Low voltage measurement design

AD5933 has 4 levels of output excitation voltages ranging from 200 mV p-p to 2 V p-p. However, for some bio-impedance measurement applications, 200 mV is still too high. To attenuate the excitation voltage at the transmit side of AD5933 (VOUT side), an operational amplifier with low output resistance, AD8608, is chosen to build an attenuation stage.

Figure A- 19 is the schematic of the low voltage circuit. The attenuation amplifier buffers the unknown impedance from the effects of R_{out} and introduces a smaller output impedance in series with $Z_{unknown}$ [13]. The ratio of $R1/R2$ determines the attenuation rate. For example, with the values of $R1=25\text{ k}\Omega$ and $R2=100\text{ k}\Omega$, the 200 mV p-p excitation voltage will be attenuated by $\frac{1}{4}$. A much lower voltage (50 mV p-p) will be applied across the capacitive sensing sensor. To increase accuracy of the measurement, the RFB resistor should be carefully selected to utilize the full ADC resolution.

3.1.3 Peripherals

SSD1306 128×32 I2C OLED is selected as the display of the system. A 4-pin push button (controlled by PIN10) is used to control the start of a test. 3×4 matrix keypad (connected to PIN3~9) is adopted allowing customizing the frequency and voltage parameters of a test.

3.1.4 Multichannel

Control of AD5933 is carried out via I2C-compliant serial interface protocol [37] and one AD5933 has a default 7-bit serial bus slave address, 0x0D. The ACEK multichannel system needs more than 10 AD5933 to work synchronously. Arduino microcontroller has a single I2C bus if not expanded by software solutions. One software solution is to use an alternative library. However, software I2C extension need to tie up additional pins of Arduino other than SDA and SCL, and many of the sensor and display libraries for I2C devices have a dependency upon the Wire library, we can't Wire on the same sketch when using the alternative library for I2C expansion [38]. For these reasons, a hardware solution by I2C multiplexer, TCA9548A, is adopted in this work.

Two TCA9548APWR working with 16 channels of AD5933 impedance converter in total is shown in Figure A- 20. One TCA9548APWR address is the default value '000'(serial bus address: 0x70) when A0 (pin1) A1 (pin 2) and A2 (pin 21) are grounded. The other I2C multiplex address is set to '100'(serial bus address: 0x71) by connecting A0 (pin 1) to high (VDD).

Due to the global chip shortages, the impedance converter chip AD5933 is out of stock nationwide so we were not able to get enough chips to do a full test. In the test, three AD5933 impedance converters in total (two of which are selected via the first I2C multiplex and the rest one by the second multiplex) are set to work together. By printing out each impedance reading of each channel to the serial port and by enabling timestamp in the Serial Monitor tool, we can calculate the time required for one impedance measurement. As a result, the time period for one measurement (including switching the I2C channel, updating the AD5933 control register, reading the AD5933 data register, and serial printing the reading) is 31ms on average. Theoretically, the system could finish all readings of the 16 channels one by one within one second. Thus, by adding a delay between each reading, we can control the time period between each measurement.

3.1.5 Power module

The Arduino microcontroller-based system can be powered by 5V USB connection. However, the maximum power delivery as well as the maximum output current of USB 2.0 is limited. The 5V USB is not able to power the multichannel bio-impedance test system when all the 16 channels are involved, thus output power is necessary. On the other hand, 9V battery instead of USB port is used when it is used as a portable device. Thus, the voltage regulator is designed for both systems.

The processor of Adafruit Feather M0 is 3.3V logic and the board contains a 3.3V regulator with 500 mA peak current output. As the operation voltage of Arduino Mega 2560 microcontroller as well as regular Arduino display OLED is 5 V, a 5 V voltage regulator is necessary when the system is powered by a battery.

The impedance measurement chip AD5933 can work in 5V or 3.3V power supply. However, the 3.3V supply voltage has a much lower power consumption. The typical I_{DD} for AD5933 (work in Normal Mode) of 3.3V V_{DD} is 10mA. The current increased to 17mA when using 5V supply voltage. Low drop voltage regulator LD1117AS33TR is used in this design which can provide up to 800 mA of output current.

3.1.6 PCB design of the system

Figure A- 22 and Figure A- 23 are the 2D and 3D layouts of the designed PCB of the multichannel ACEK capacitance sensing system. According to the schematic (Figure A- 16 and Figure A- 17), while AD5933 is measuring impedance, the additional gain and phase between the AD5933 VOUT pin and the excitation voltage delivered by the external amplifiers could be calibrated as system noise. Thus, to shorten the signal wire length between the amplifiers and the IDE sensors, all the amplifiers are placed near the edge connector.

3.1.7 Coding

AD5933 returns a complex output code for the real (R) and imaginary (I) components of Discrete Fourier Transform (DFT) by two registers. Notice that the R and I values read from the registers are not the real and imaginary values of corresponding resistance and capacitive reactance of a series RC circuit. Instead, the magnitude of the impedance can be calculated by

$$Z_{unknown} = \frac{1}{Gain\ Factor \times \sqrt{R^2 + I^2}} \quad 3.2$$

where the *Gain Factor* is calculated via the method shown in Figure A- 16 and is calibrated by

$$Gain\ Factor = \frac{\left(\frac{1}{Z_{cal}}\right)}{\sqrt{R^2 + I^2}} \quad 3.3$$

The impedance measurement coding of the ACEK sensing system is based on Arduino IDE, an open-source library for AD5933 from the GitHub website is adopted [39].

The library is enough to get impedance readings, but there are two missing features stated by the author: 1. Configure the AD5933 excitation range; 2. Calibrate the phase of the system (in the calibration process) so that the phase of impedance readings can be analyzed.

The default output voltage level is 2 V p-p, which is too high for small impedances from ACEK biosensors. Moreover, the high voltage could break the biomolecules. By modifying the library as well as adding codes to the main function, the output excitation voltage range can be configured and selected by the user through a keypad.

The phase readings of an impedance are meaningless without system phase calibration. Thus, the impedance readings are incorrect when capacitors are involved, which is not feasible for ACEK interfacial capacitive sensing. Phase calibration, calculated by $Phase(\text{rads}) = \tan^{-1}(I/R)$ while using a calibration resistor (pure resistance), is done in this work. The phase of unknown impedance is calculated simply by $\phi_{unknown} = \phi_{measured} - \phi_{system}$, which is the measured value minus the calibrated system phase value. The reactive component value, which represents the capacitor value in this work, is extracted by the following equation:

$$Cap = \frac{1}{-2\pi f(Z \times \sin(\phi))} \quad 3.4$$

Besides the above two deficiencies of the open-source code, another key function that needs to be realized in coding is to control the time period of each measurement. For regular applications, the time duration of one measurement doesn't matter as long as the readings are correct. However, as ACEK target enrichment is contributed to the output AC voltage signals on IDE sensors, the time period is important. Corresponding codes are added to the frequency sweep function so that the time period between each impedance measurement point can be configured.

After configuring the time of measurements (e.g., 15 seconds in total for a measurement of 15 points), the capacitance change rate (dC/dt) is calculated via Least Squares Regression.

The flowchart of the coding is shown in Figure A- 24(a). When the “main” function is called as we power up the Arduino-based system, the void setup () and void loop () functions are automatically called. After the variables are declared or initialized, the setup() function will be called and executed for once. When the setup() function exits, the loop() function will be called and executed again and again unless the Arduino board is powered

off or has been restarted. The user customizes and system calibration is done in the setup() function so that it will only execute once. The testing process, on the other hand, is placed in the loop() function to allow multiple measurements. A push-button is used to allow users to pause the next measurement and to change sensors between two measurements.

3.1.8 Sequenced measurement

While the basic coding shown in Figure A- 24(a) does allow users to customize the frequency and voltage level of an ACEK capacitive sensing, the parameters are fixed in one test. In some situations when the user would like to switch the voltage level (or frequency) to manipulate the probe/target molecules, a different design for sequenced measurement is needed.

For example, in one experiment, the researcher needs to switch from a higher voltage level (phase 1) to a lower voltage level (phase 2). The higher voltage level is for the association purpose so that all particles including target and interference molecules will be absorbed to the electrodes. On the other hand, when the voltage level is lowered down in the second phase, dissociation happens. The target molecules which are binding with the probes will keep on the electrodes whereas the interference molecules will be released. Capacitance changes in the first phase reflect how many particles are associated and changes in the second phase indicate how many of them are interference molecules.

It is easy to re-configure voltage (or frequency) levels after one sweep. The sequenced measurement is realized by running two sweeps with different register configurations. However, the calibrations must also be done by two different sweeps with additional storage space for gain & phase return values from the second sweep. Figure A- 25 illustrates the quick switch of voltage level from range 1 to range 3 in a period less than 10 ms. Figure A- 24(b) shows the workflow of one sequenced measurement example.

3.2 Potential based detection system

Analog inputs of the Arduino microcontroller board can be used to collect voltage signals of sensors. As introduced in section 1.2, potentiometric sensors and MOS gas sensors all

yield voltage signals when working with the measuring circuit. This section focuses on the design of an electronic nose system based on Arduino microcontroller board. As voltage difference generated by potentiometric sensor is much smaller than those by the MOS gas sensing circuit, an additional FET circuit is designed in this section.

3.2.1 Circuits

A low-cost portable signal acquisition system for gas sensor array is built based on a commercial microcontroller and integrated circuit (IC) chips. Figure A- 26 is a schematic of the voltage signal acquisition system. The data acquisition process is controlled by an Arduino® Feather M0 bluefruit microcontroller. The whole system is powered by 9 V DC voltage, easily becoming battery powered when necessary. The 9 V voltage is then shifted to 5 V and 3.3 V through a voltage regulator to power the sensor array and the microcontroller.

3.2.2 Laboratory setup

A gas detection experimental system based on the MOS sensor array is designed. To simulate the air environment in the indoor ventilation system, a laboratory glove box is used. Figure A- 27 (b) shows the CLEATECH® 2300 series containment glove box used in this work. The glove box includes an intake & exhaust filter and an adjustable speed 480 CFM impeller blower unit, which allows the simulation of different air velocities. A paper pipe (diameter: 12cm, length: 90 cm) is used to guide the airflow. As shown in Figure A- 27 (a), the sensor array is located on the right side of the paper pipe in the glove box, whereas the test gas is added to the other side by syringe. The right access door of the glove box keeps closed all the time, whereas the left door keeps open during the test to guarantee the same air pressure in the inner and outer box.

Voltage signals of the MOS gas sensor array are obtained reflecting the sensor resistance change caused by chemical reactions. The sampling rate is set to 10 Hz.

3.2.3 Selection of gas sensors

Several factors are considered when choosing sensors for the array, high sensitivity; fast response; high stability and reusability; low power consumption; low cost; minimum number of sensors. Table A- 1 shows the operating conditions and sensitivity characteristics of the HANWEI[®] MQ series and Figaro[®] TGS series gas sensors used in this work. These are the widely used low-cost MOS sensors (less than \$20) from the two major manufacturers selling e-nose products. Specific gases reacting with the sensing elements will lead to a change in the sensor resistance, and voltage signals related to these MOS gas sensors are used to indicate the presence of target gases.

Voltage signals of the gas sensors are obtained by the ARM[®] Cortex M0 microcontroller. The sampling rate is set to 10 Hz (i.e 10 sample points per second). Instead of directly measuring the sensor resistances themselves, the data acquisition board measures the voltage across a load resistor that is connected in series with the sensor. An increase in the measured voltage would be observed when the sensor resistance decreases during the gas reaction. Figure A- 28(a) shows voltage signals of the 6 different sensors when 4 ml 8.3% acetone in the air is added to the left inlet of the tube shown in Figure A- 27. Random noise present in the original signal is removed by wavelet denoising. As previously mentioned, the MOS gas sensor has a cross-sensitivity characteristic, leading to a rather non-ideal selectivity. As reported in ref. [40], when a sensor is exposed to a VOC mixture, the gas with higher reactivity will dominate the reaction with the adsorbed oxygen at the surface of the metal oxide. Take the response of the Figaro[®] TGS2602 sensor as an example. As shown in Figure A- 28(b), when testing single gas of acetone (2 ml, 8.3%) or ethanol (10 ml, 1.74%), the peak voltages for the two single gas tests are around 1.2 V and 1.9 V. When the same amounts of the two gases are mixed and tested, the peak value of the mixed gas response is not equal to the sum of the two single gas test outputs. The peak voltage of the VOC mixture is less than 2.5V, much lower than the combined single gas results. The baselines of the three signals in Figure A- 28(b) are removed to highlight the differences in peak values. This indicates that using one single MOS gas sensor or a simple calculation

cannot recognize VOC mixtures in air, thus an array of different sensors with a pattern recognition algorithm is needed.

Considering the total power consumption of the sensor array, the number of sensors should be minimized. Therefore, correlation coefficients and principal component analysis (PCA) are used next to identify and exclude the sensors with duplicate responses. Table A-2 shows the correlation coefficients between each pair of sensors. The signals used here and in the following PCA section are the same as shown in Figure 2(a). The largest correlation coefficient is 0.9855, which happens between MQ 136 and TGS 2610 sensor, followed by the correlation coefficient between TGS 2600 and TGS 2602. The larger a correlation coefficient is, the more similar the signals of the sensor pair are. A close to 1 correlation coefficient means that one of the sensors is redundant.

PCA is a mathematical procedure that transforms a number of correlated variables into a number of principal components (PC) that are uncorrelated or orthogonal to each other. The PC loadings are the correlation coefficients between the variables (signals of the different gas sensors) and factors (principal components). [41]

The first 6 rows of Table A- 3 are the principal component loadings, and the last row is the percentage of the total variance explained by each principal component. It can be seen from the last row that the first principal component (PC1) explained about 96% of the whole information, and the second principal component (PC2) explained about 3.8% of it. The rest four principle components contained less than 0.2% of the information. Thus, we should select sensors based on the first two PCs.

To select a subset of variables (sensors), we should find out which original variables (sensor signals) have the highest correlations with the first two principal components. The maximum three loadings for PC1 and PC2 fall on TGS 2602 (PC1-0.9332), MQ 136 (PC1-0.2510, PC2-0.7081), TGS 2610 (PC1-0.1997, PC2-0.5234), and TGS 2611 (PC2-0.3113). This implies MQ 135 and TGS 2600 are less important for PC1 and PC2, and can possibly be removed without loss of information.

Figure A- 29 shows the sensors' responses to the same amount of acetone, ethanol, and IPA. Unlike the other 5 sensors whose responses to ethanol and IPA are larger than

their response to acetone, TGS 2602 has a larger response to acetone when the same amount of gas is tested. This means that TGS 2602 is the key sensor to distinguish acetone from ethanol or IPA when used with any other sensors in this array. In contrast, the responses of MQ 135 to all three gases are very small while the noise is much larger than other sensors. Notice that the signal processing in this section is done on PC by MATLAB[®] R2018b. Combining the above information, MQ 135 and TGS 2600 are removed from the array.

3.2.4 Sample acquisition

Liquid acetone (CH₃)₂CO, isopropyl alcohol CH₃CHOHCH₃ (IPA), and ethanol CH₃CH₂OH used in this work are certified ACS grade purchased from Fisher Scientific (USA). The temperature of the laboratory keeps at 23±1°C during experiments. The humidity of the environment keeps at 50±5 RH% during the experiments. The original concentrations of acetone, IPA, and ethanol gases in a 1 L gas chamber under experimental conditions are 8.3%, 1.71%, 1.74% in air respectively. Gas samples for tests are extracted from the headspace using a syringe operated by hand. When more than one VOC is used, the syringe is shaken for 10 seconds to get a gas mixture. Airflow in the glovebox remains unchanged during the test, by keeping the settings of both the indoor ventilation system and the fan speed of the glovebox the same all the time. As shown in Figure A- 28(a) and Figure A- 29, the response and recovery time of the MOS gas sensors we chose for our test are within 1 minute. This enables a relatively high measurement frequency when continuous monitoring is required.

3.2.5 Extended-Gate FET readout circuit for Potentiometric sensing

Potentiometric sensing of Pb²⁺ ions by the all-solid-state ISE sensor obeys the Nernst equation, which predicts a linear dependence of voltage response on the logarithm of the activity (concentration) of the ions [25]. Theoretically, as two electrons are involved, the maximum slope of the voltage signal is $59.16mV/2 = 29.58mV$ per decade, which is relatively small for analog input pins to read directly. As introduced in 1.2.2, potentiometric sensing measures the oxidation-reduction potential difference between two electrodes

when no current is present, equipment of high input impedance is required. To extract the small potential of the ISE sensor, an extended-gate FET readout circuit with matched MOSFET pair is designed for potentiometric sensing.

Matched Pair MOSFET array, ALD1106, is chosen for differential sensing. As shown in Figure A- 30, two channels of ISE sensors are connected to the gate terminals of the MOSFET pair. Drain voltages are then measured by analog input pins of the Arduino board. The output voltage from the potentiometer, shown by the port 'ref_bias' in Figure A- 30, is used to bias the sensors to make it work at a designed region of the MOSFET, thus, avoiding the use of a DC voltage source. Figure A- 31 shows the experimental setup of the extended-gate FET readout system for potentiometric sensors.

According to the output characteristics from the datasheet, when $V_{GS} < 2V$, ALD1106 MOSFET meets the saturation requirement at $V_{DS} \geq 2V$ [42]. The MOSFET works in the saturation region so that the drain current (I_D) is controlled by the gate voltage. The transfer curve of ALD1106 (Figure A- 32) is tested by Keithley® 2450 and 2401 source meter. It shows that when V_{GS} is lower than 700mV, I_D is still under the control of V_{GS} even when V_{DS} lowered to 1V. The bias resistor at the drain terminal is optimized to be 180k Ω so that when the gate terminal is biased and working at 400 mV ~ 600 mV, the voltage at the drain terminal changes accordingly in a range between 5V~1.5V.

Similar to the electronic nose system designed in this research, signal processing of the FET readout system shown in this thesis is done via PC. MATLAB & Arduino serial communication is used to visualize the collected voltage in real-time (Figure 3.18). To be a real portable system, on-chip signal processing, as well as LED display, are need.

The fabricated Pb^{2+} ISE sensor has an original potential of about 40 mV (in 10 mM $NaNO_3$ buffer solution) when using an Ag/AgCl electrode as a reference electrode. To make the MOSFET work near the subthreshold region, a bias of 400 mV is added to the reference electrode via a potentiometer. Figure A- 34 shows the measurement results of two hand-made ISE sensors through the designed MOSFET readout system. The Pb^{2+} and Cd^{2+} ion sensors have selectivity issues that need improvements. However, the test does show us the feasibility of the designed Arduino microcontroller based FET readout system.

3.3 Integration of multi-mode sensing

The two modes of potential based detection introduced in this section all use analog input of the microcontroller board to measure voltage output. As the presence of both the two kinds of target analyte (VOCs in gas phase and heavy metal ions in liquid sample) all show a sudden increase of voltage, and the Arduino microcontroller board has a few analog input pins, it is easy to integrate them into one system. Moreover, as the multichannel ACEK capacitive sensing based impedance readout is through I2C communication, it can be integrated with the potential based detection as well. Figure A- 35 shows the design of the integrated multi-mode sensing system.

CHAPTER 4

MEASUREMENTS AND DETECTION RESULTS

4.1 ACEK measurements

4.1.1 System calibration test

The calibration process of the system is done with a $1.2\text{k}\Omega$ resistor as calibration impedance ($Z_{\text{CAL}}=1.2\text{k}\Omega$) and another known $1.2\text{k}\Omega$ resistor as test impedance ($Z_{\text{UNKNOWN}}=1.2\text{k}\Omega$). As shown in Figure A- 36, the calibration test should show a result of $1.2\text{k}\Omega$ or close to $1.2\text{k}\Omega$ in normal conditions. It is worth to mention that when a pure resistive load is measured, the deviation of the readings is relatively small at any frequencies from 1kHz to 100kHz . However, the maximum capacitive load the buffer amplifier (AD8608, UA1 in Figure A- 18) can drive without oscillation is 1000pF . Thus capacitive load greater than 1000pF will cause oscillation, which will result in incorrect impedance readings with large deviation. This issue could be avoided by adding a resistive component to the load to maintain stability. For example, when the system is calibrated with a $1.2\text{k}\Omega$ resistor at 100kHz , resonance happened when trying to measure the impedance of a 2700pF capacitor at this frequency. As shown in Figure A- 37, abnormal impedance readings were observed on the 2700 pF capacitor. By adding a 910Ω resistor in series with the 2700pF capacitor, the oscillation disappeared, and the deviation of the impedance readings back to normal (standard deviation $\sigma < 1\Omega$). In a real test, as the impedance of an IDE biosensor is also not pure capacitive, e.g. 1000Ω resistance with 3000pF capacitance when using the RC series model, the system should work normally without oscillation.

4.1.2 Impedance measurement

Figure A- 38 is a photo of the ACEK impedance readout system. The performance of the system is then represented by the measurements on a series of impedances composed of different resistors and capacitors (Figure A- 39).

4.2 VOC gas measurements

In a steady-state measurement, signals are obtained after the stimulus is introduced and allowed to reach equilibrium and after all sensors of the electronic nose have reached steady-state responses. On the other hand, when the stimulus is present only for a short duration, which is usually 20-30 seconds, the signals obtained are transient signals, and such events can only be captured by transient measurement [43]. Therefore, in this research, transient measurement is chosen to realize near real-time monitoring of VOCs in the air.

4.2.1 Feature extraction and selection

Signals of a gas sensor array depend on the gas chemical information as well as the geometries of the measurement system. The design of the measurement system, such as the geometries of the measurement chamber and the arrangement of the sensors in the chamber, along with the chemical makeup of the gas flow, would affect the signals obtained. It is clear that not all the information obtained is useful for gas identification. Instead, only a portion of the signal carries relevant chemical information [44]. The main idea of feature extraction is to extract relevant information from the response curve with less redundancy.

A typical transient response of a gas sensor, a response curve of the TGS2602 sensor in phase space, is shown in Figure A- 40 (a). The obtained transient sensor response is labeled as “S.”. The most popular feature obtained from this kind of signal is the signal maximum S_0 , which is the magnitude difference between its peak and baseline. Besides the signal maximum, the time from the beginning of the signal to its peak T_p is also widely used [43].

While the features in the time domain are simple and fast to compute, more information can be potentially extracted from the signals using more sophisticated features. The first derivative of the sensor response has been used in the literature [45]. As the sensor response S may reflect the concentration level of the adsorbed oxygen, the first derivative signal of S may reflect the concentration change rate of the adsorbed oxygen [45]. Sensor

signal behavior in phase space could be represented by an orthonormal basis formed by S and dS/dt signals [44].

Figure A- 40 (b) and (c) show the transient signals of the MOS sensors to the three VOC gases. The three parameters extracted are: $\max(dS/dt)$, the maximum of the derivative signal; $\min(dS/dt)$, the minimum of the derivative signal; a/b , the location of $\max(dS/dt)$. The values of the above parameters are determined by the amount of VOC that reached the sensor surface, as shown in Figure A- 40 (b), a larger amount of gas will result in a higher $\max(dS/dt)$ value. While the shapes of the response curve between ethanol and acetone are similar on TGS 2602, we can notice the difference in shape on MQ 136. In Figure A- 40 (c), MQ 136 sensor has flatter response curves to different amounts of acetone gas when compared with its responses to ethanol gas.

4.2.2 Classification algorithms and results

Both ethyl alcohol and isopropyl alcohol are alcoholic compounds with similar physical and chemical properties. Ethyl alcohol is a primary alcohol with -OH attached to the first carbon. Isopropyl alcohol is a secondary alcohol with -OH attached to the second carbon. Ethanol is found in alcoholic drinks while isopropyl is toxic when ingested. Although it is easy to distinguish acetone from the two alcoholic compounds directly by the features we have extracted, the differences between ethanol, IPA, and its mixtures are hard to notice. A backpropagation neural network with one hidden layer and one output layer is used to classify the VOC samples. The use of a single hidden layer guarantees a short training time. The input data of the network has 20 dimensions, which is composed of 5 features for each of the 4 sensors in the array. Figure A- 41 shows the topological structure of the neural network. The 20 inputs represent the 20-dimensional feature. W and b in the hidden layer and the output layer represent the weights and thresholds of the 10 sigmoid hidden neurons and the 7 softmax output neurons. The seven true or false outputs (with only one to be true at once) give the predicted class of the VOC gas.

The VOC samples can be divided into 7 classes: single gas of acetone (class 1), ethanol (class 2), IPA (class 3); binary mixture of acetone & ethanol (class 4), acetone &

IPA (class 5), ethanol & IPA (class 6); and ternary mixture of acetone, ethanol, and IPA (class 7). The single and binary gas has 15 samples for each class, and the ternary gas has 60 samples. The total 150 samples are randomly divided into three parts: 70% (104 samples) for training, 15% (23 samples) for validation, and 15% (23 samples) for testing. The classification accuracies of training, validation, and testing are 85.6%, 87.0% and 82.6%, respectively.

Figure A- 42 shows the overall confusion matrix of the classifier. The numbers (1 to 7) in both horizontal/vertical axis of the confusion matrix represents seven different target/output classes. The numbers in the diagonal (marked in green color) are the number of correctly predicted samples of each class. Other blocks are wrong predictions. The percentage numbers at the right side and bottom of the table indicate the percentage of correct (green) or wrong (red) predictions of that row or column. The overall accuracy is 85.3%.

MATLAB & Arduino serial communication is used to visualize as well as monitor the signals in real-time. The BPNN based training model is pre-saved as a user-defined classification function. When a reaction is detected, the features are extracted, and the parameters are sent to the classification function. Since the transient signal features are extracted in a short time (compared with steady-state signal), the result of the classification is printed within 1 minute after the gas reached the sensor surface.

4.2.3 Regression algorithms and results

Regression algorithms aim to model the relationships between the input features and the target output in order to predict an output value for new input data [46]. The target output is called the response variable and the input feature is called the predictor variable. When more than one feature is used in a regression model, the model is called a multivariate regression. Least squares regression is a way to find the best fit curve for a set of data points. It works by minimizing the sum of the squares of the residuals (a residual is the difference between an observed response and the predicted response provided by the model). Depending on whether or not the function giving the residuals is linear, least squares

problems fall into two categories: linear least squares and nonlinear least squares. According to Chen et.al [47], nonlinear activation functions in the BPNN are better than linear functions in VOC concentration estimation. Here, multivariate and multioutput regression based on neural network is applied to estimate the amount of each of the three different gases in the binary or ternary gas mixture. The regression network also has 20 inputs, which is the same as the classifier in the above section. 14 sigmoid hidden neurons are used in the hidden layer. The output layer has 3 linear neurons. Instead of having 7 true or false output targets, the regression network has 3 numeric targets. The three continuous output parameters are the estimated concentrations of the three VOCs in the tested VOC mixtures.

In this work, 120 samples in total (60 binary mixtures and 60 ternary mixtures) are randomly divided into three groups, with 84 samples for network training, 18 samples for validation, and 18 samples for testing. Levenberg-Marquardt (LM) algorithm is applied in the network training to solve the non-linear least squares problem. Training automatically stops when the mean square error (MSE) of the validation samples starts to increase.

To illustrate the performance of the BPNN detection, Figure A- 43 (a) and (b) compares the overall regression result by multivariate linear regression and the BPNN based regression. In Figure A- 43, each symbol ('o', 'x' or '*') represents a regression point of ethanol, IPA, or acetone. It can be seen that the BPNN method offers a lower average error than the linear regression method. MSE of the three VOC gas by BPNN regression is 0.054 ml for acetone (in the range of 0-2 ml), 1.06 ml for ethanol (in the range of 0-10 ml), and 1.33 ml for IPA (in the range of 0-10 ml).

CHAPTER 5

CONCLUSIONS

This work presents the design of low-cost portable electroanalytical detection systems based on Arduino microcontroller board. The achievements include:

- Observation of ACEK phenomenon on IDE sensors. Even though the ACEK theory is well-established, the phenomena vary on different electrodes with different AC signals (frequency and amplitude), media solutions (e.g. permittivity, viscosity), as well as particles (e.g. size, shape, dielectric properties). IDE sensor of 100 μm gap/width is one of the most simple but frequently used designs in ACEK capacitive sensing. AC signals of frequencies ranging from 1kHz to 100kHz with PBS or SSC as buffer solution are normal for ACEK biosensing technique. The use of 1 μm fluorescent particles as well as 3~4 μm live yeast cells in these experiments clearly show us how particles in liquid react to AC signals, which illustrates the ACEK capacitive sensing mechanisms.
- Multichannel ACEK capacitive sensing system with a 16-channel microsensor array is designed. The AC signals used for AECK process are easily customized by the user when the system is powered up. Moreover, an additional circuit is designed for some biosensing applications where lower excitation voltage is required.
- Electronic nose system based on MOS gas sensors for qualitative and quantitative analysis of VOC gas in indoor ventilation system is built in this work. The classifications on acetone, ethanol, isopropyl alcohol gas as well as its binary and ternary gas mixtures yielded acceptable results.
- All-solid-state ISEs for heavy metal ions detection is fabricated. Extended-gate FET circuit combined with Arduino microcontroller board is designed for potentiometric sensing. Tests with the hand fabricated all-solid-state ISE sensors are executed and the feasibility of this design is verified.

REFERENCES

- [1] G. N. Meloni, "Building a Microcontroller Based Potentiostat: A Inexpensive and Versatile Platform for Teaching Electrochemistry and Instrumentation," *The American Chemical Society and Division of Chemical Education*, vol. 93, no. 7, pp. 1320-1322, 2016.
- [2] W. Gao, X. Luo, Y. Liu, Y. Zhao and Y. Cui, "Development of an arduino-based integrated system for sensing of hydrogen peroxide," *Sensors and Actuators Reports*, vol. 3, 2021.
- [3] A. J. Hanson, "Portable Electrochemical System for Flexible Hybrid Electronics," Western Michigan University, Master's Theses, 2019.
- [4] Z. Li, "Arduino Based Environmental Air Monitoring System," CASE WESTERN RESERVE UNIVERSITY, Master Theses, 2017.
- [5] C. Perez-Gonzalez, C. Salvo-Comino, F. Martin-Pedrosa and L.Dias, "Analysis of Milk Using a Portable Potentiometric Electronic Tongue Based on Five Polymeric Membrane Sensors," *Frontiers in Chemistry*, 2021.
- [6] J. Wu, C. Cheng, Q. Yuan, R. Oueslati, J. Zhang, J. Chen and R. Almeida, "Simple, Fast And Highly Sensitive Detection Of Gram-Negative Bacteria By A Novel Electrical Biosensor," in *Annu Int Conf IEEE Eng Med Biol Soc*, 2018.
- [7] J. Meng, J. Huang, R. Oueslati and J. Wu, "A single-step DNAzyme sensor for ultra-sensitive and rapid detection of Pb²⁺ ions," *Electrochimica Acta*, vol. 368, 2021.
- [8] C. Cheng, S. Wang, J. Wu, Y. Yu, R. Li and S. Eda, "Bisphenol A Sensors on Polyimide Fabricated by Laser Direct Writing for Onsite River Water Monitoring at Attomolar Concentration," *Applied Materials & Interfaces*, vol. 8, pp. 17784-17792, 2016.
- [9] X. Liu, C. Cheng, J. Wu, S. Eda and Y. Guo, "A low cost and palm-size analyzer for rapid and sensitive protein detection by AC electrokinetics capacitive sensing," *Biosensors and Bioelectronics*, vol. 90, pp. 83-90, 2017.

- [10] R. Oueslati, "Development of a smart bio-diagnostic platform for point-of-care detection by multiplexed electrokinetic sensing," University of Tennessee, PhD diss, 2019.
- [11] "Volatile Organic Compounds' Impact on Indoor Air Quality," United States Environmental Protection Agency (EPA), [Online]. Available: <https://www.epa.gov/indoor-air-quality-iaq/volatile-organic-compounds-impact-indoor-air-quality>. [Accessed 2 December 2019].
- [12] A. Dey, "Semiconductor metal oxide gas sensors: A review," *Materials Science and Engineering: B*, vol. 229, pp. 206-217, 2018.
- [13] N. Miura, H. Minamoto, G. Sakai and N. Yamazoe, "New-type calorimetric gas sensor using temperature characteristics of piezoelectric quartz crystal fitted with noble metal catalyst film," *Sensors and Actuators B: Chemical*, vol. 5, no. 1-4, pp. 211-217, 1991.
- [14] W. Weppner, "Solid-state electrochemical gas sensors," *Sensors and Actuators*, vol. 12, no. 2, pp. 107-119, 1987.
- [15] T. Töpfer, K. P. Petrov, Y. Mine, D. Jundt, R. F. Curl and F. K. Tittel, "Room-temperature mid-infrared laser sensor for trace gas detection," *Applied Optics*, vol. 36, no. 30, pp. 8042-8049, 1997.
- [16] T. ISHIHARA and S. MATSUBARA, "Capacitive Type Gas Sensors," *Journal of Electroceramics*, vol. 2, no. 4, pp. 215-228, 1998.
- [17] A. J. Ricco, S. J. Martin and T. E. Zipperian, "Surface acoustic wave gas sensor based on film conductivity changes," *Sensors and Actuators*, vol. 8, pp. 319-333, 1985.
- [18] Y. Xu, X. Zhao, Y. Chen and W. Zhao, "Research on a Mixed Gas Recognition and Concentration Detection Algorithm Based on a Metal Oxide Semiconductor Olfactory System Sensor Array," *sensors*, vol. 18, no. 10, 2018.

- [19] G. Łagód, S. M. Duda, D. Majerek, A. Szutt and A. D.-S. Łódka, "Application of Electronic Nose for Evaluation of Wastewater Treatment Process Effects at Full-Scale WWTP," *Processes*, vol. 7, no. 251, 2019.
- [20] A. Blanco-Rodríguez, V. F. Camara, F. Campo, L. Becheran, A. Duran, V. D. Vieira, H. d. Melo and A. R. Garcia-Ramirez, "Development of an electronic nose to characterize odours emitted from different stages in a wastewater treatment plant," *Water Research*, vol. 134, pp. 92-100, 2018.
- [21] M. Cuartero and G. A. Crespo, "All-solid-state potentiometric sensors: A new wave for in situ aquatic research," *Current Option in Electrochemistry*, vol. 10, pp. 98-106, 2018.
- [22] S. Komaba, T. Akatsuka and K. Ohura, "All-solid-state ion-selective electrodes with redoxactive lithium, sodium, and potassium insertion materials as the inner solid-contact layer," *Analyst*, vol. 142, pp. 3857-3866, 2017.
- [23] X. Liu, C. Cheng and J. Wu, "A low cost and palm-size analyzer for rapid and sensitive protein detection by AC electrokinetics capacitive sensing," *Biosensors and Bioelectronics*, vol. 90, pp. 83-90, 2017.
- [24] A. Bratov and N. Abramova, "Chemical sensors and biosensors based on impedimetric interdigitated electrode array transducers," in *Smart Sensor and Sensing Technology*, New York, Nova Science Publishers, 2013, pp. 155-164.
- [25] M. Cosio and S. Benedetti, "Potentiometric Sensor," *Chemical Analysis of Food: Techniques and Applications*, 2012.
- [26] "Wikipedia/Potentiometric sensor," [Online]. Available: https://en.wikipedia.org/wiki/Potentiometric_sensor. [Accessed 12 Jan. 2022].
- [27] J. Hu, A. Stein and P. Buhlmann, "Rational design of all-solid-state ion-selective electrodes and reference electrodes," *Trends in Analytical Chemistry*, vol. 76, pp. 102-114, 2016.

- [28] "Operating principle-MOS type," Figaro USA, Inc., [Online]. Available: <http://www.figarosensor.com/technicalinfo/principle/mos-type.html>. [Accessed 3 Dec 2019].
- [29] Wikipedia, "Capacitive sensing," [Online]. Available: https://en.wikipedia.org/wiki/Capacitive_sensing.
- [30] D. Wang, F. Li and Z. Shuai, "Electrochemical interfacial capacitance in multilayer graphene sheets: Dependence on number of stacking layers," *Electrochemistry Communications*, vol. 11, no. 9, pp. 1729-1732, 2009.
- [31] N. Wan, Y. Jiang, J. Huang, J. Wu and X. Lin, "Rapid and Sensitive Detection of miRNA Based on AC Electrokinetic Capacitive Sensing for Point-of-Care Applications," *Sensors*, vol. 21, no. 12, 2021.
- [32] J. Wu, "Interactions of electrical fields with fluids:laboratory-on-a-chip applications," *IET Nanobiotechnol*, vol. 2, no. 1, pp. 14-17, 2008.
- [33] Wikipedia, "Dielectrophoresis," [Online]. Available: [https://en.wikipedia.org/wiki/Dielectrophoresis#:~:text=Dielectrophoresis%20\(DEP\)%20is%20a%20phenomenon,the%20presence%20of%20electric%20fields](https://en.wikipedia.org/wiki/Dielectrophoresis#:~:text=Dielectrophoresis%20(DEP)%20is%20a%20phenomenon,the%20presence%20of%20electric%20fields) ..
- [34] M. Z. Bazant, "AC Electro-Osmotic Flow," in *Encyclopedia of Microfluidics and Nanofluidics*, Springer, 2008.
- [35] J. Huang and J. Wu, "Review of Non-invasive Continuous Glucose Monitoring Based on Impedance Spectroscopy," *Sensors and Actuators A Physical*, vol. 311, no. 12, 2021.
- [36] R. Keim, "ALL ABOUT CIRCUITS/Applications of the Op-Amp: Voltage Follower Circuit," 20 September 2020. [Online]. Available: <https://www.allaboutcircuits.com/video-tutorials/op-amp-applications-voltage-follower/>. [Accessed 11 Jan. 2022].

- [37] "Analog devices technical documentation/datasheets," [Online]. Available: <https://www.analog.com/media/en/technical-documentation/datasheets/AD5933.pdf>. [Accessed 09 01 2022].
- [38] D. Workshop, "Multiple I2C Buses with an Arduino," [Online]. Available: <https://dronebotworkshop.com/multiple-i2c-bus/>. [Accessed 09 01 2022].
- [39] mjmeili, "GitHub/arduino-ad5933," 05 4 2021. [Online]. Available: <https://github.com/mjmeili/arduino-ad5933>. [Accessed 11 2021].
- [40] L. Zhao, X. Li, J. Wang, P. Yao and S. A. Akbar, "Detection of Formaldehyde in Mixed VOCs Gases Using Sensor Array With Neural Networks," *IEEE SENSORS JOURNAL*, vol. 16, no. 15, pp. 6081-6086, 2016.
- [41] 14 10 2007. [Online]. Available: <ftp://statgen.ncsu.edu/pub/thorne/molevoclass/AtchleyOct19.pdf>. [Accessed 1 1 2020].
- [42] Advanced Linear Devices, Inc., [Online]. Available: <https://www.aldinc.com/pdf/ALD1116.pdf>. [Accessed 17 01 2022].
- [43] L. Carmela, S. Levyb, D. Lancetc and D. Harel, "A feature extraction method for chemical sensors in electronic noses," *Sensors and Actuators B: Chemical*, vol. 93, pp. 67-76, 2003.
- [44] E. Martinelli, C. Falconi, A. D'Amico and C. D. Natale, "Feature Extraction of chemical sensors in phase space," *Sensors and Actuators B*, vol. 95, pp. 132-139, 2003.
- [45] S. Zhang, C. Xie, M. Hu, H. Li, Z. Bai and D. Zeng, "An entire feature extraction method of metal oxide gas sensors," *Sensors and Actuators B*, vol. 132, pp. 81-89, 2008.
- [46] R. Bali and D. Sarkar, *R Machine Learning By Example*, Birmingham: Packt Publishing, 2016.

- [47] Z. Chen, Y. Zheng, K. Chen, H. Li and J. Jian, "Concentration Estimator of Mixed VOC Gases Using Sensor Array With Neural Networks and Decision Tree Learning," *IEEE SENSORS JOURNAL*, vol. 17, no. 6, 2017.
- [48] A. Dey, "Semiconductor metal oxide gas sensors: A review," *Materials Science and Engineering: B*, vol. 229, pp. 206-217, 2018.
- [49] X. Liu, C. Cheng, J. Wu, S. Eda and Y. Guo, "A low cost and palm-size analyzer for rapid and sensitive protein detection by AC electrokinetics capacitive sensing," *Biosensors and Bioelectronics*, vol. 90, pp. 83-90, 2017.
- [50] C. Cheng, S. Wang and J. Wu, "Bisphenol A Sensors on Polyimide Fabricated by Laser Direct Writing for Onsite River Water Monitoring at Attomolar Concentration," *ACS Applied Materials & Interfaces*, vol. 8, pp. 17784-17792, 2016.

APPENDIX

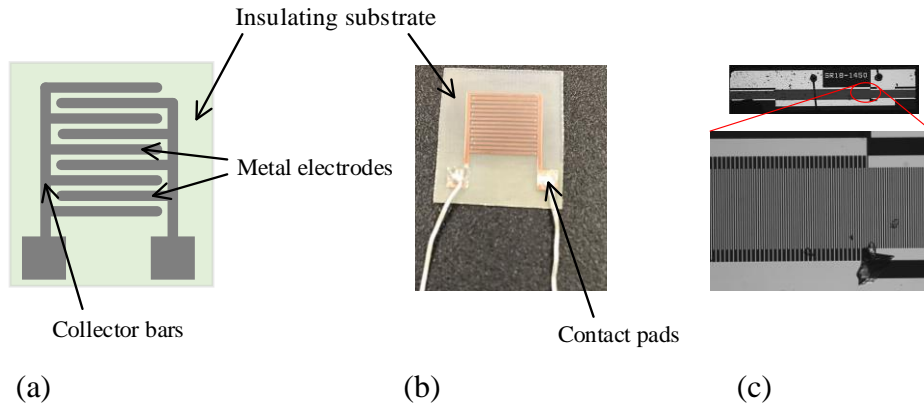


Figure A- 1. (a) a simple IDE design, (b) 200 μm width/gap hand-made IDE, (c) 2 μm width/gap SAW resonator

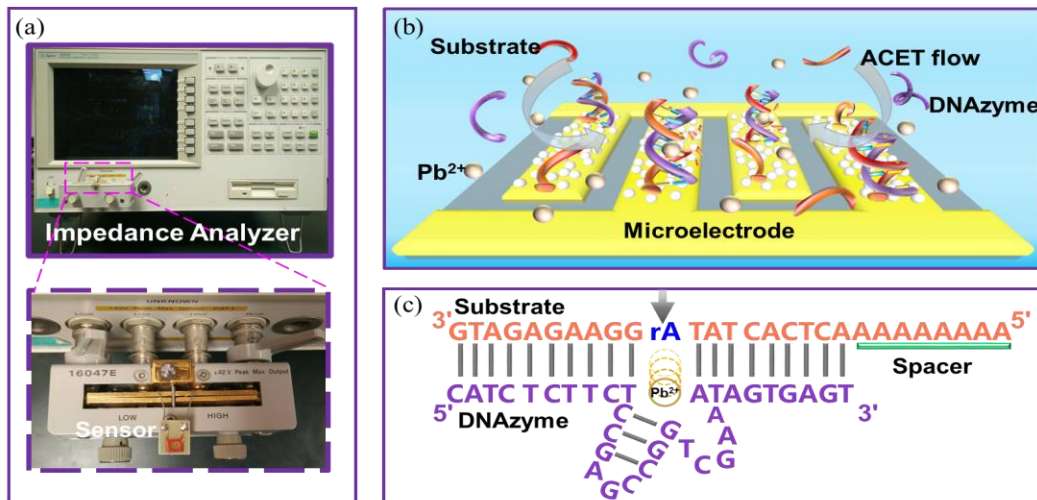


Figure A- 2. Schematic of biofluid-based DNAzyme sensor: (a) Impedance readout of the IDE sensor, (b) DNAzyme on IDE introduced by biofluid, (c) Substrate and DNAzyme sequences. (from published prior work [7])

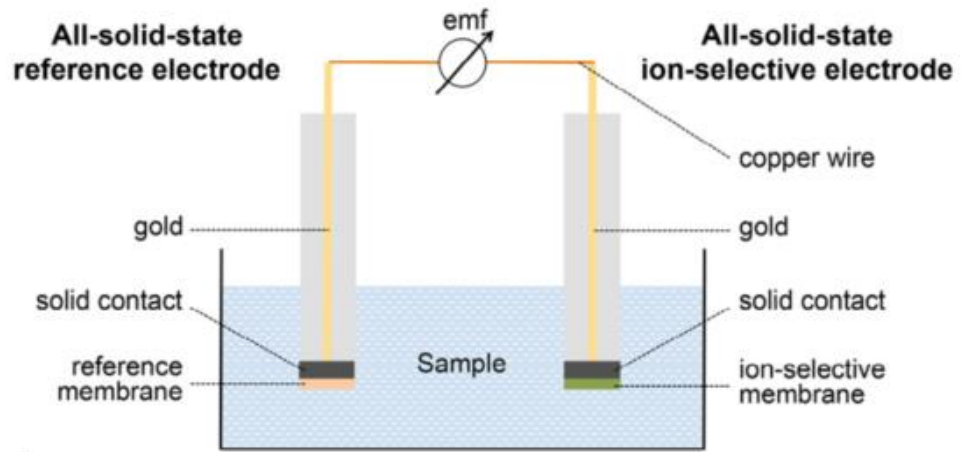


Figure A- 3. Schematic of coated-wire all-solid-state ISE and reference electrode in reference [27].

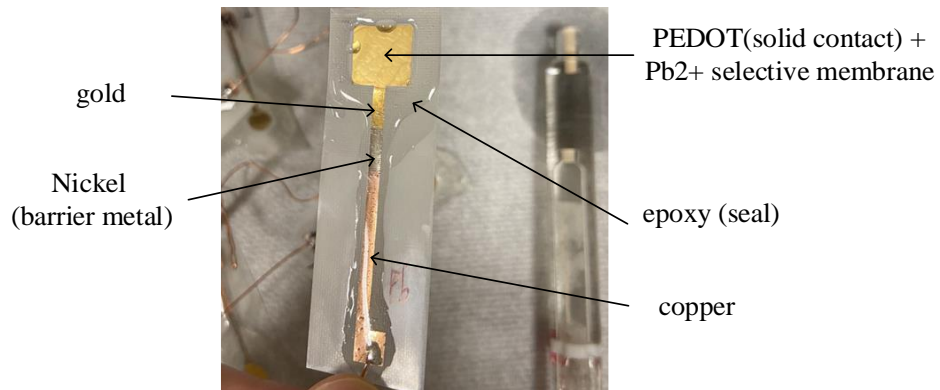


Figure A- 4. Hand-made all-solid-state Pb^{2+} ISE sensor

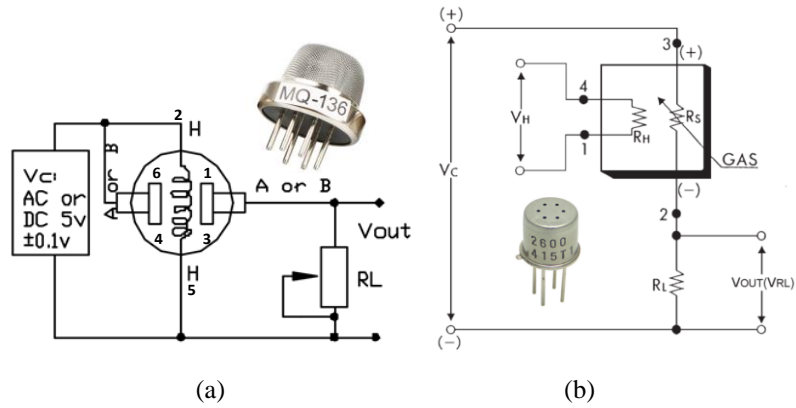


Figure A- 5. Basic measuring circuit of (a) MQ series (b) TGS series gas sensors (from datasheet)

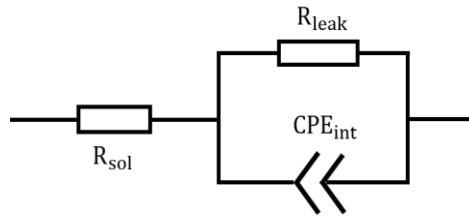


Figure A- 6. Equivalent circuit for IDE biosensor

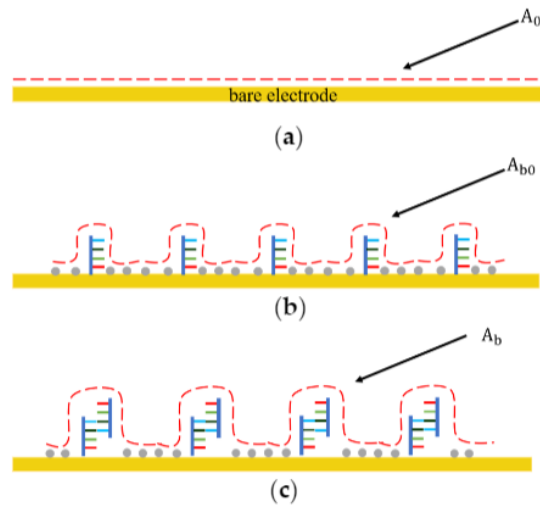


Figure A- 7. Schematic of interfacial capacitance changes at different stages, (a) before probe immobilization, (b) after probe immobilization and blocking, (c) after target binding with probe.(from published prior work [31])

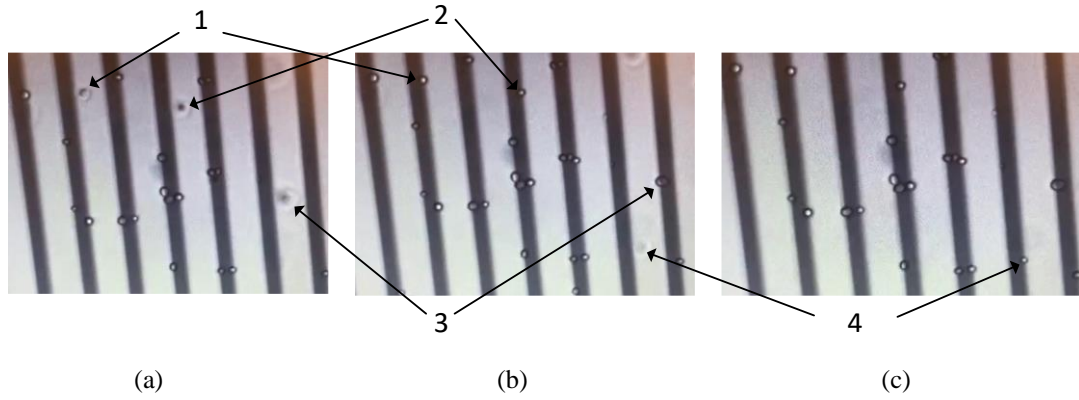


Figure A- 8. Image series show DEP force on yeast cells at 100 kHz in DI water

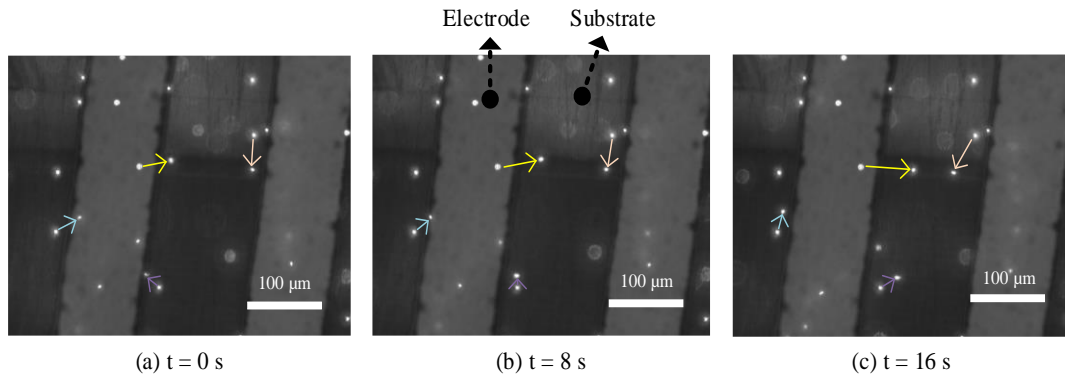


Figure A- 9. Image series show 1.0 μm fluorescent particle ACET movement at 10 kHz 0.5 \times SSC

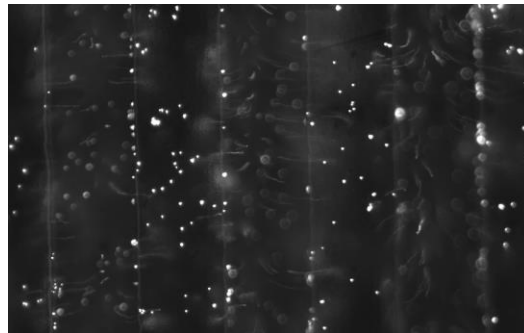


Figure A- 10. ACEO vortices shown by fluorescent particles at 100 kHz 0.1 \times PBS

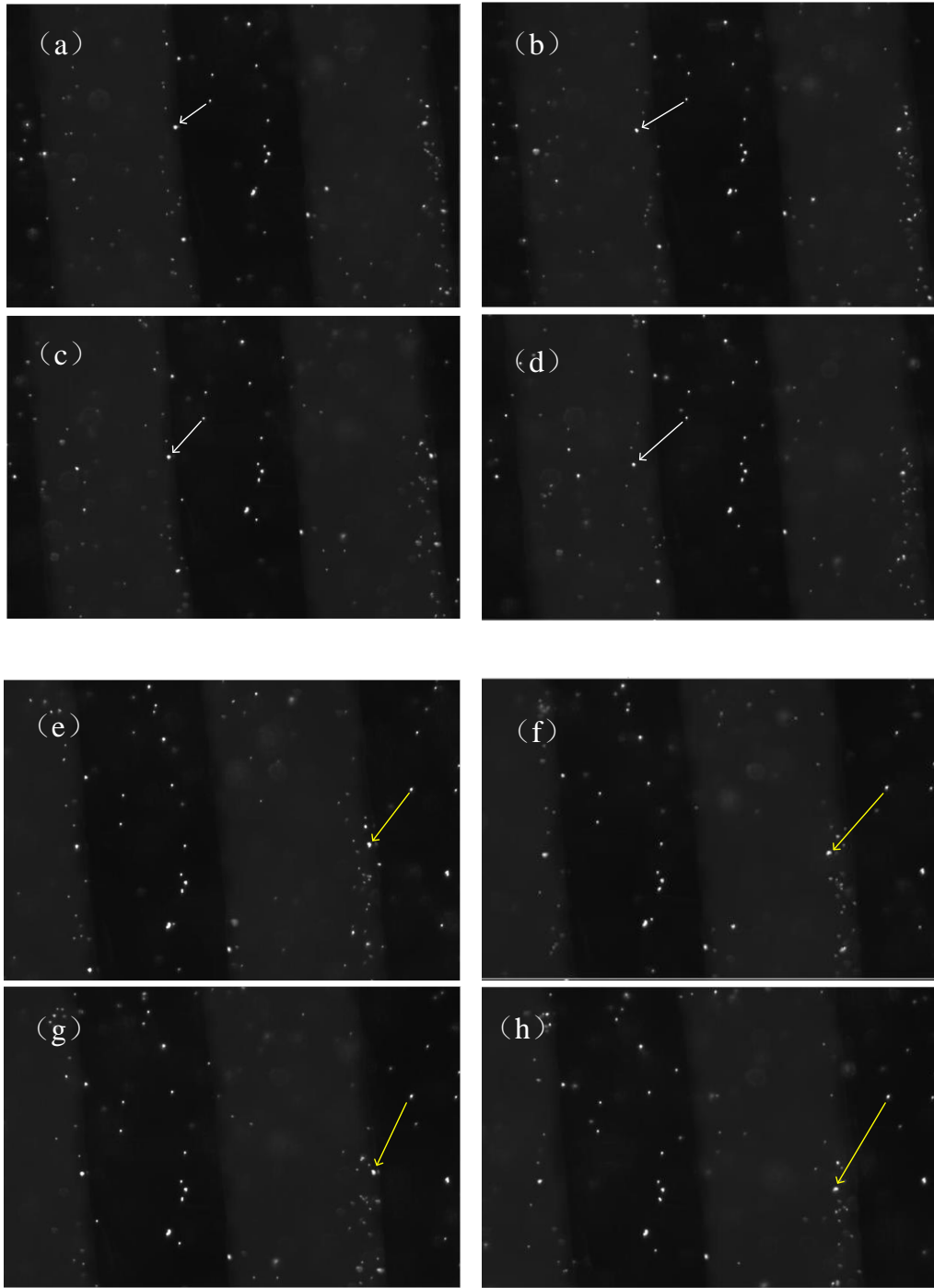


Figure A- 11. Image series showing particle movements with ACEO vortices at 10 kHz 0.1xPBS

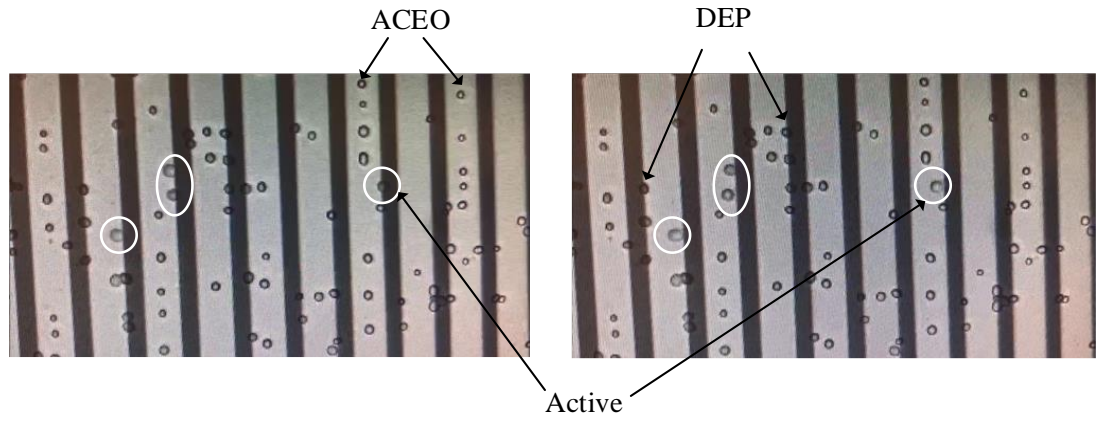


Figure A- 12. Image series showing combination of DEP and ACEO at 1 kHz in DI water

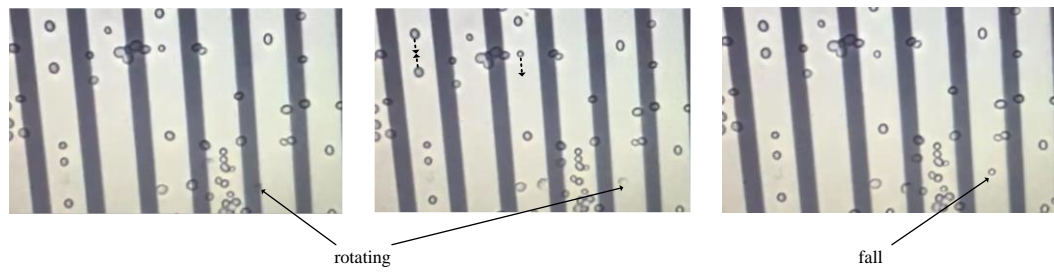


Figure A- 13. Image series showing how yeast cells move on electrode

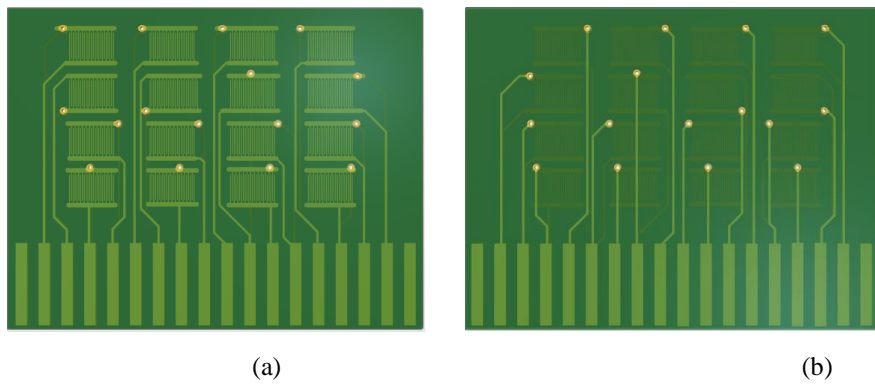


Figure A- 14. (a) Top (b) bottom view of the IDE sensor array

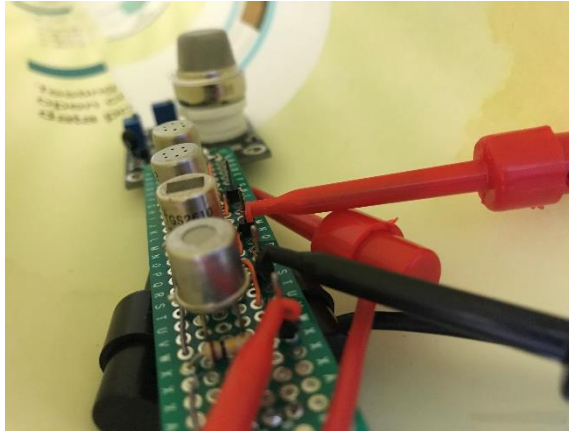


Figure A- 15. MOS gas sensor array

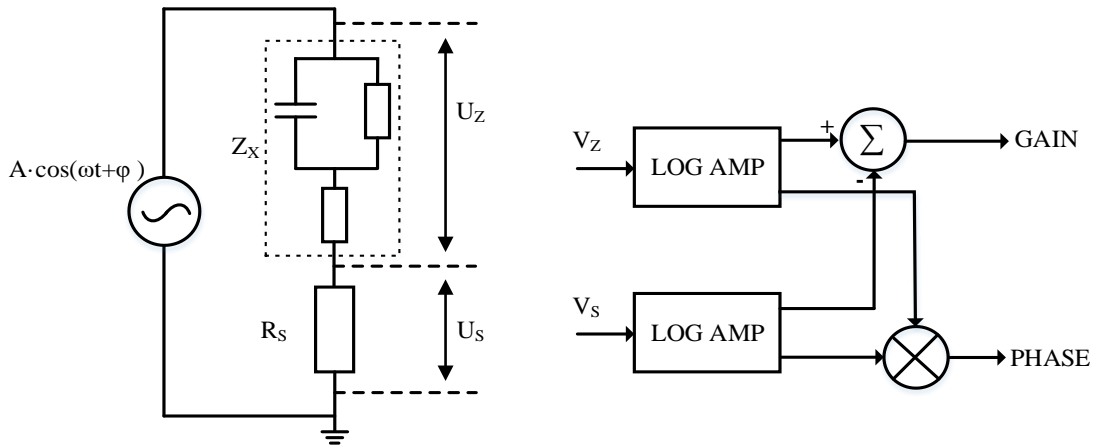


Figure A- 16. Bioimpedance measuring method. (A) Model of measurement, (B)Architecture of gain-phase detector (from published prior work [35])

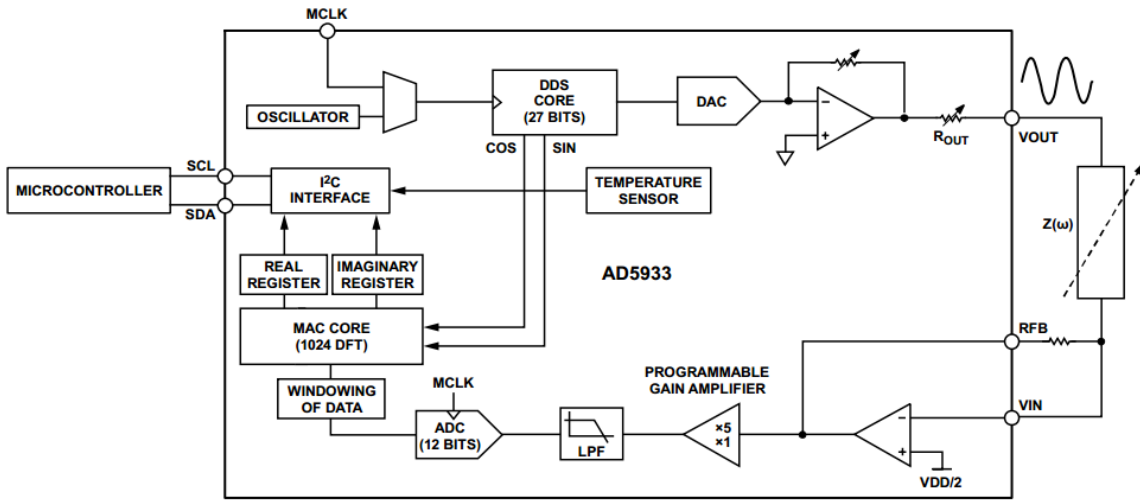


Figure A- 17. Block overview of AD5933 (from datasheet [37])

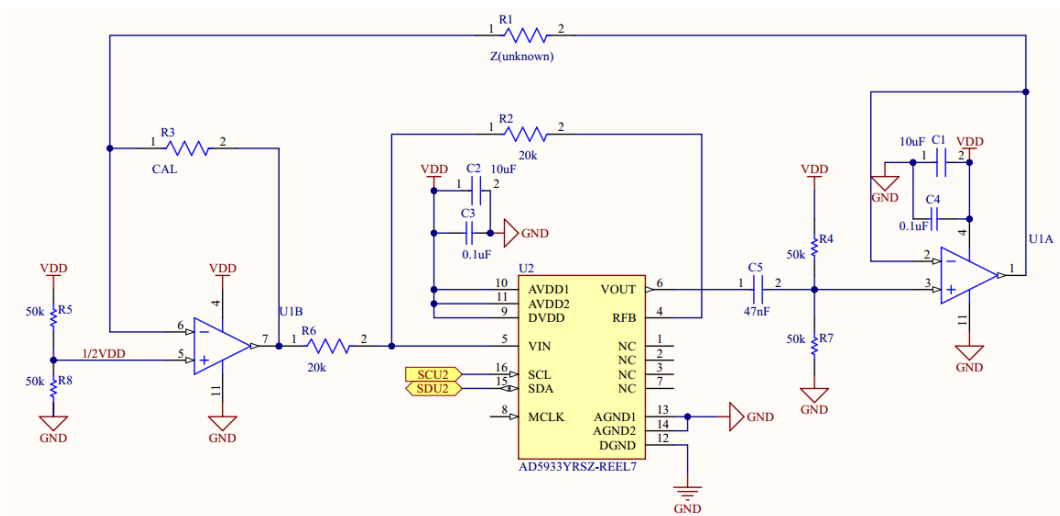


Figure A- 18. Capacitive sensing circuit

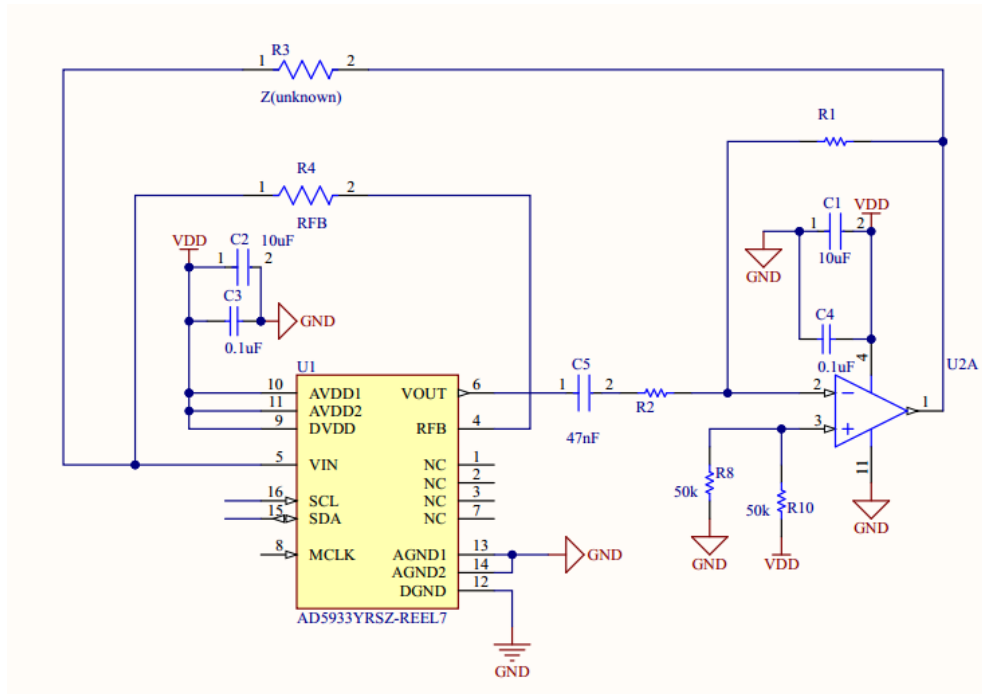


Figure A- 19. Schematic of the low voltage capacitive sensing circuit

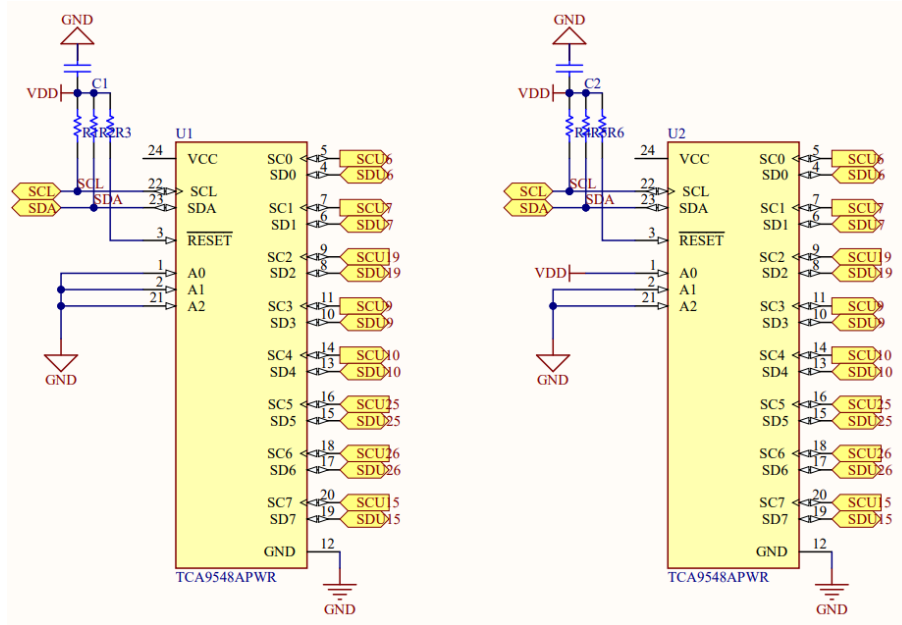


Figure A- 20. Schematic of the I2C multiplex module

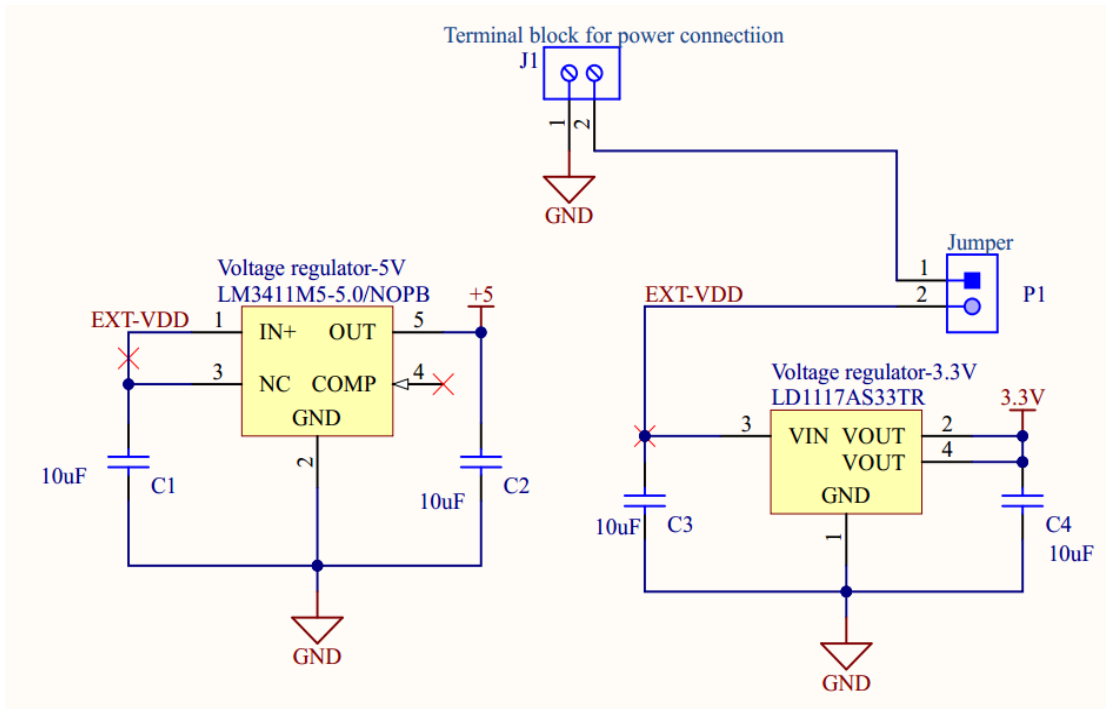


Figure A- 21 Schematic design of the power module

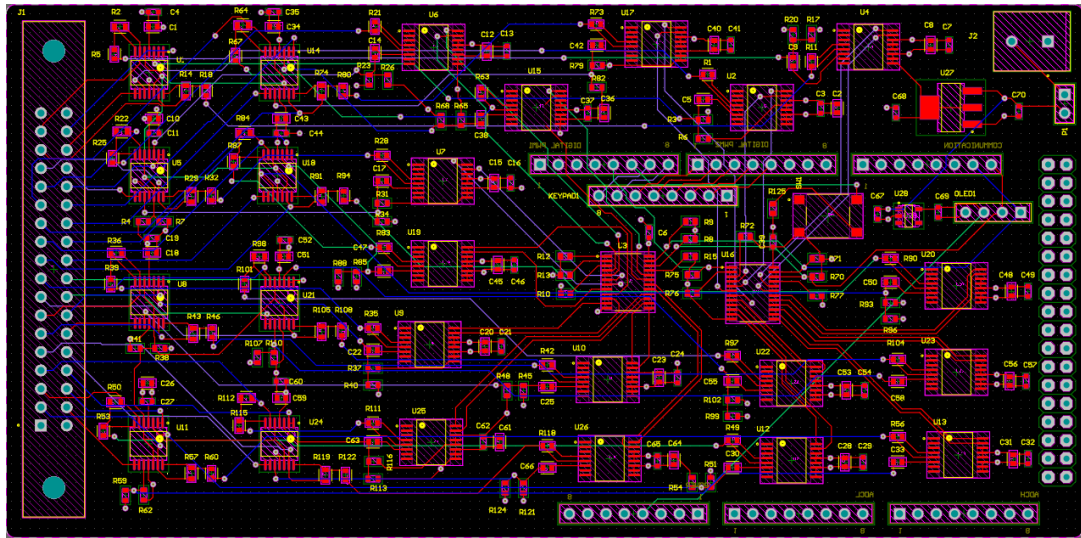


Figure A- 22. Layout of the multichannel impedance measurement system

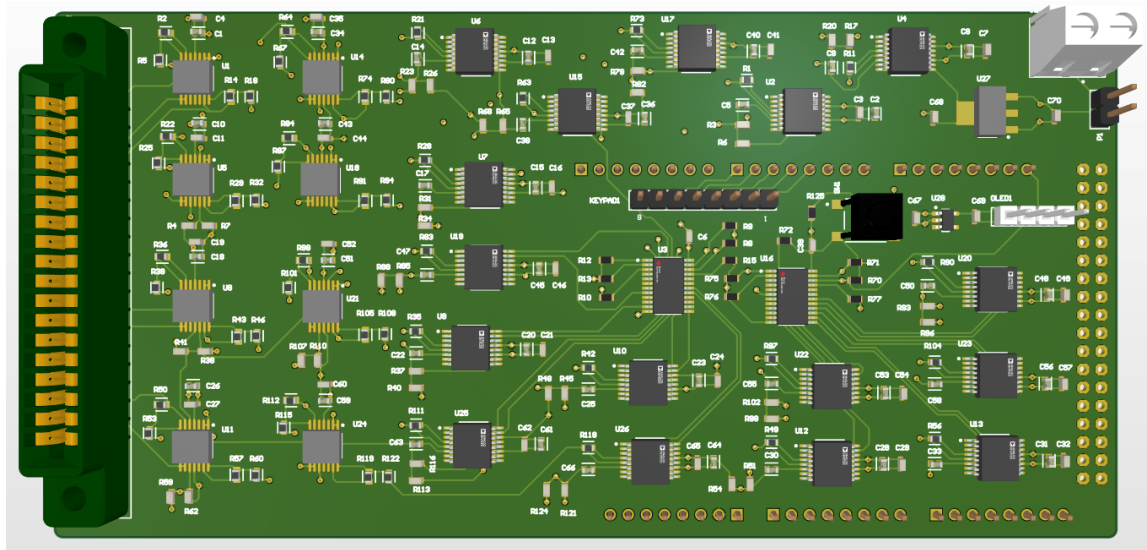


Figure A- 23. 3D layout of the multichannel impedance measurement system

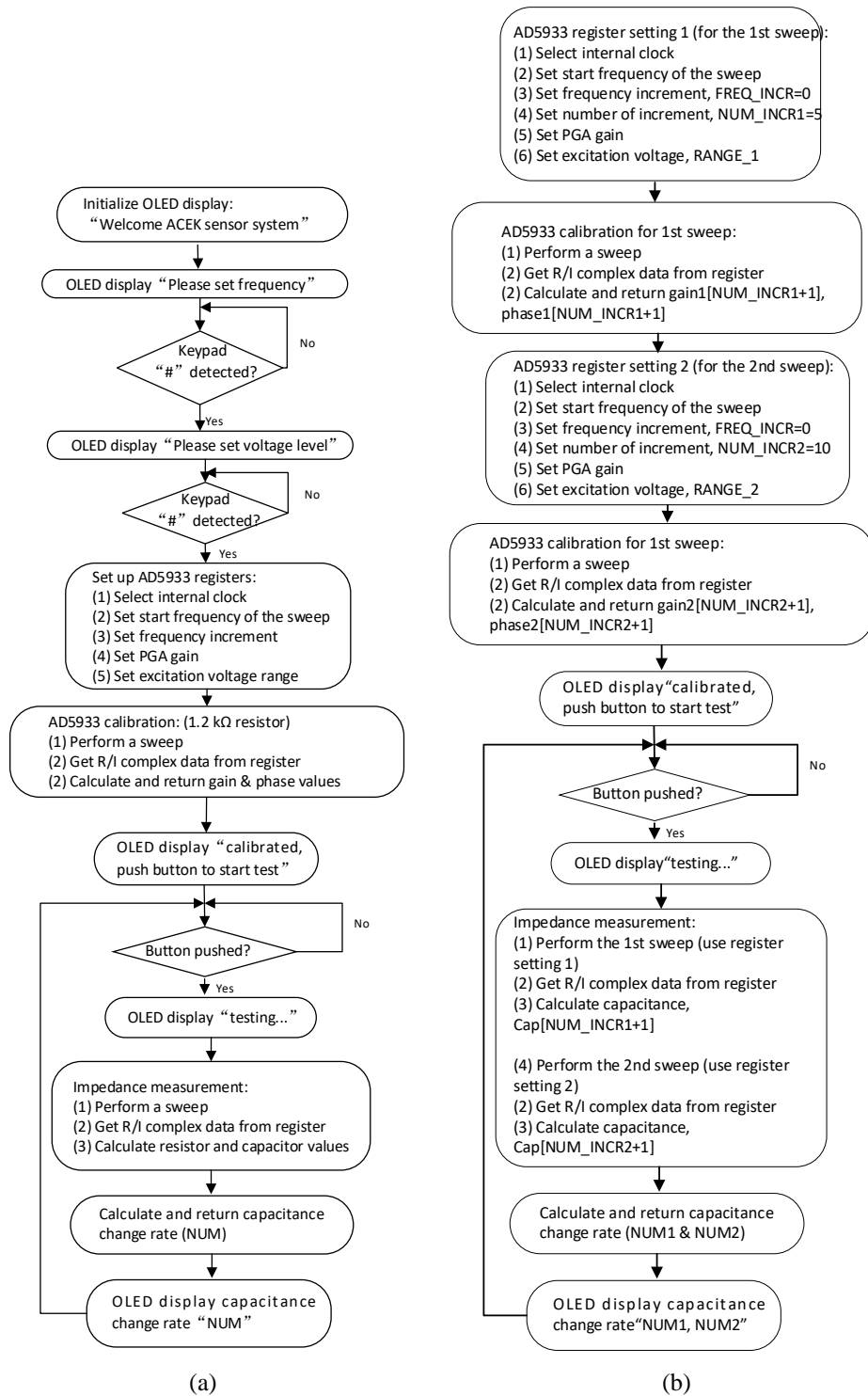
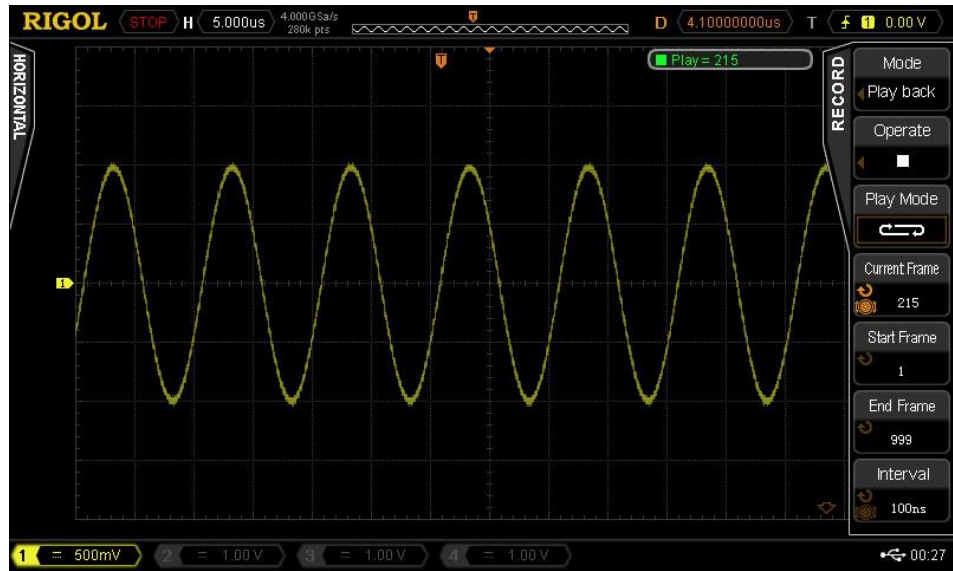
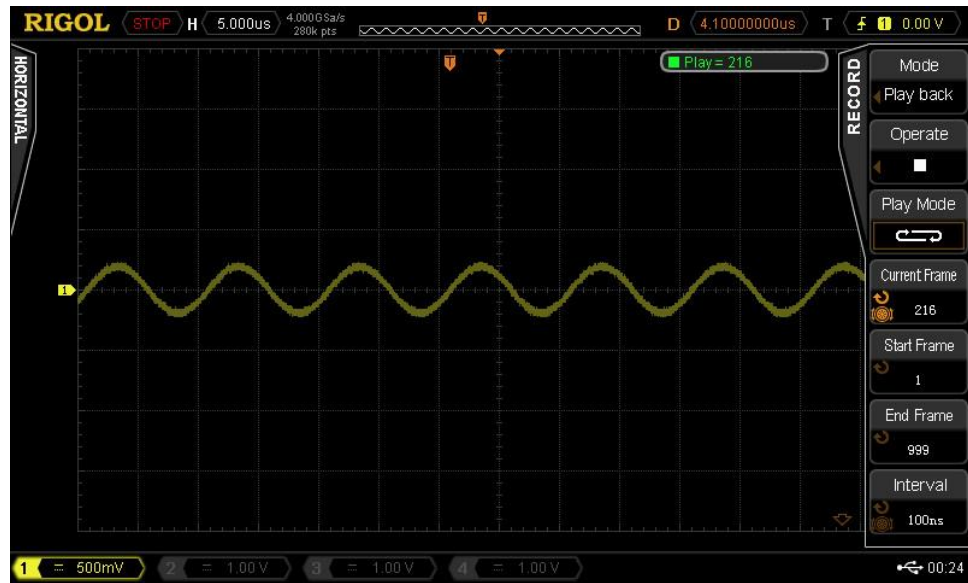


Figure A- 24. Flowchart of the ACEK biosensing system



(a)



(b)

Figure A- 25. Oscilloscope screenshot of the sequenced measurement (a) frame 215 (b) frame 216

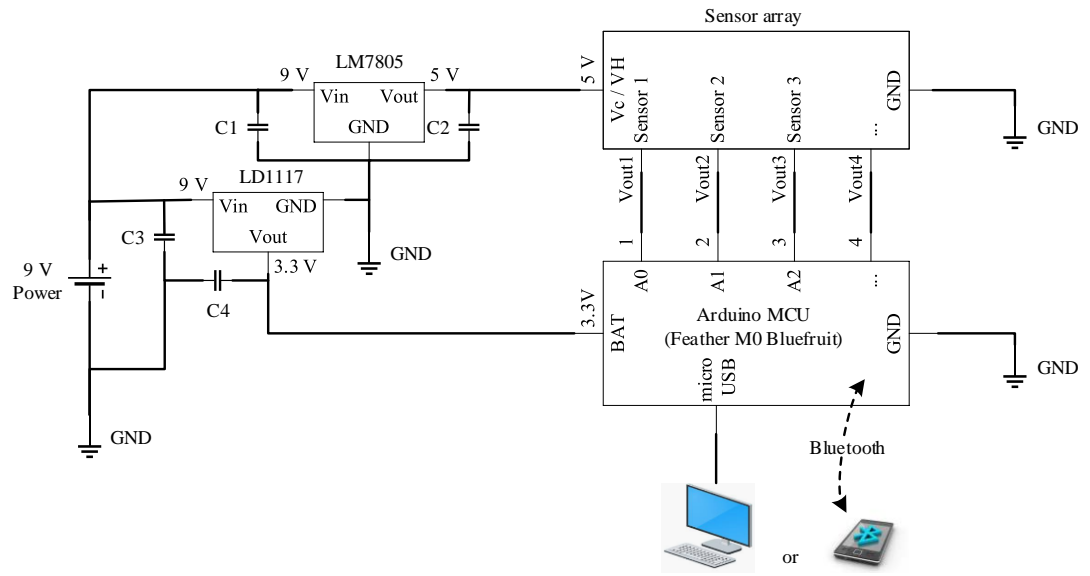


Figure A- 26. Schematic of the microcontroller-based signal acquisition system

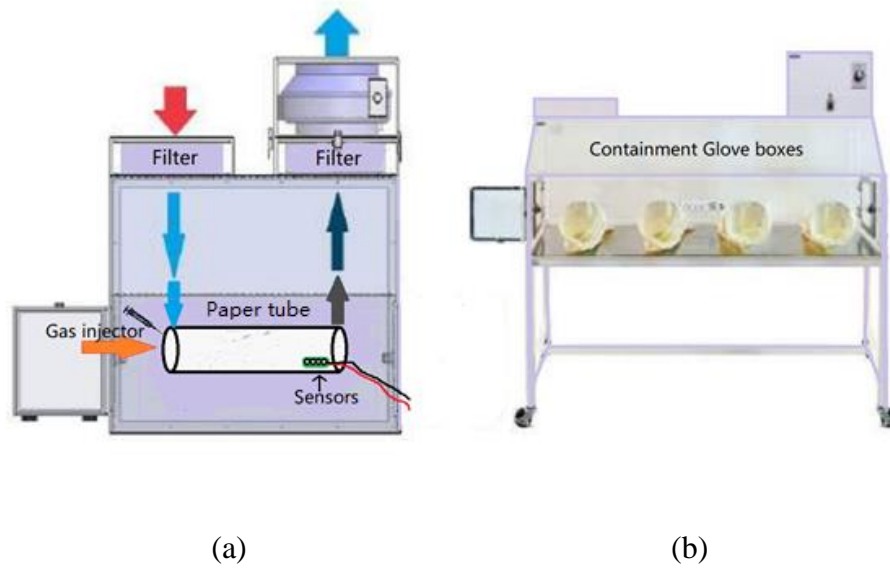


Figure A- 27 Scheme of the gas detection experimental system

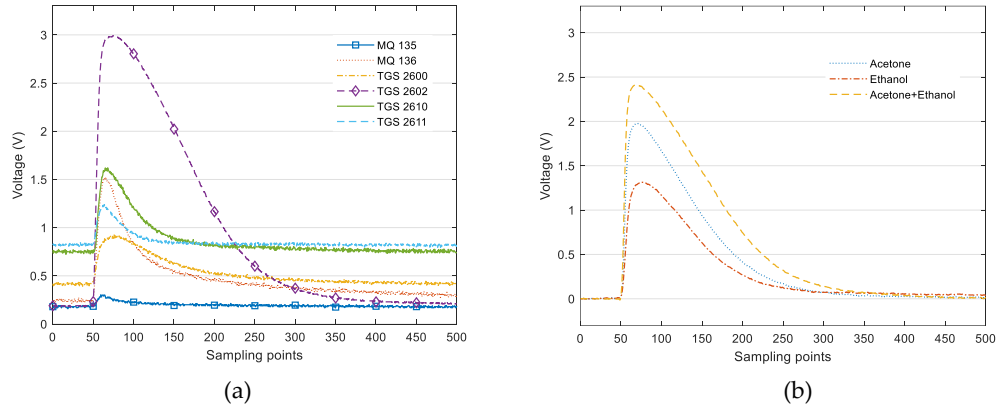


Figure A- 28 (a)Responses of the 6 MOS sensors toward acetone; (b)Single and mixed gas response curve of TGS2602. The sampling rate is 10 Hz, i.e. the x-axis is from 0 to 50 s.

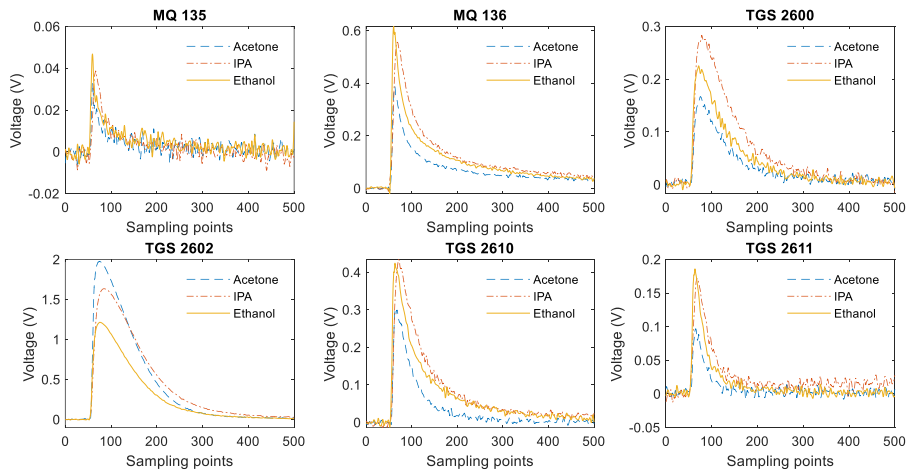


Figure A- 29 Response curve of the 6 MOS sensors to different VOCs: 2 ml of 8.3% acetone (in air); 10 ml of 1.71% IPA (in air); 10 ml of 1.74% ethanol (in air). The sampling rate is 10 Hz, i.e. the x-axis is from 0 to 50 s.

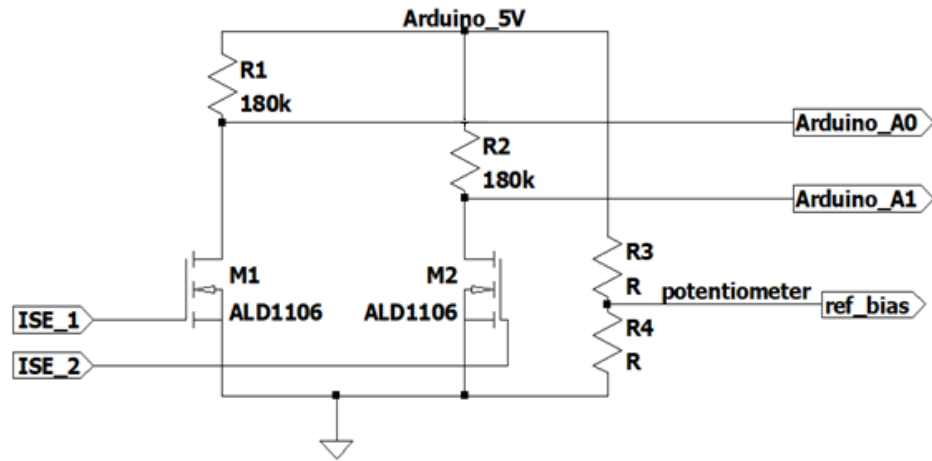


Figure A- 30. Schematic of the Extended-gate FET circuit

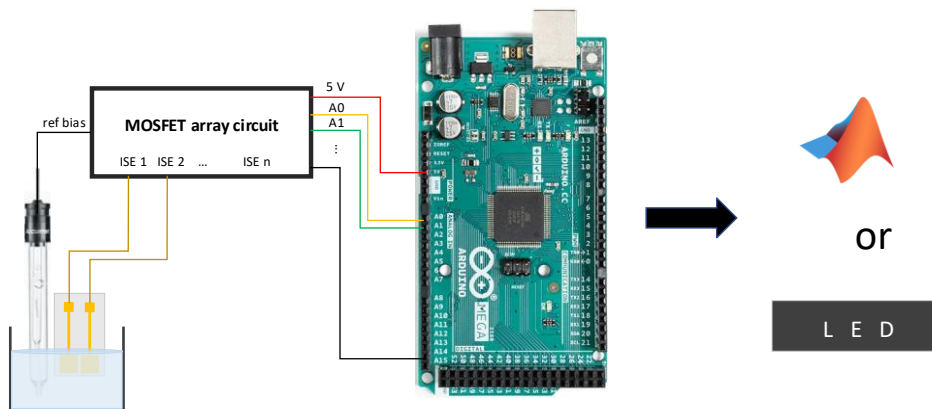


Figure A- 31. Experimental setup of the potentiometric sensing system

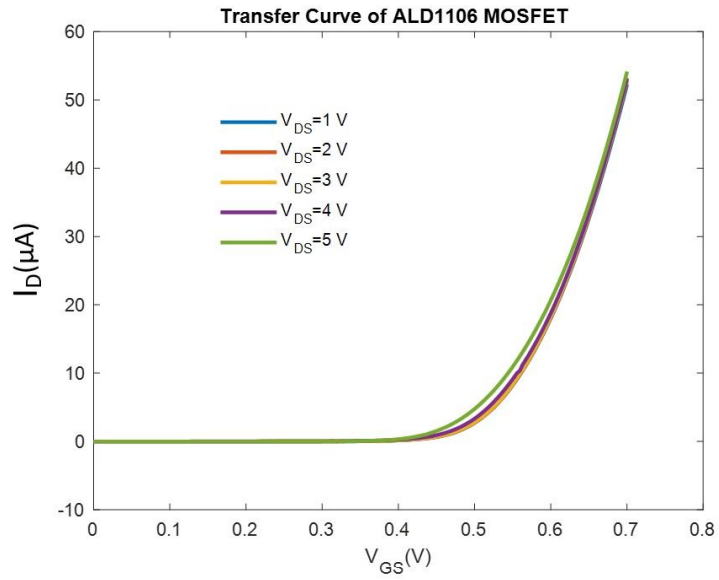


Figure A- 32. ALD1106 transfer curve

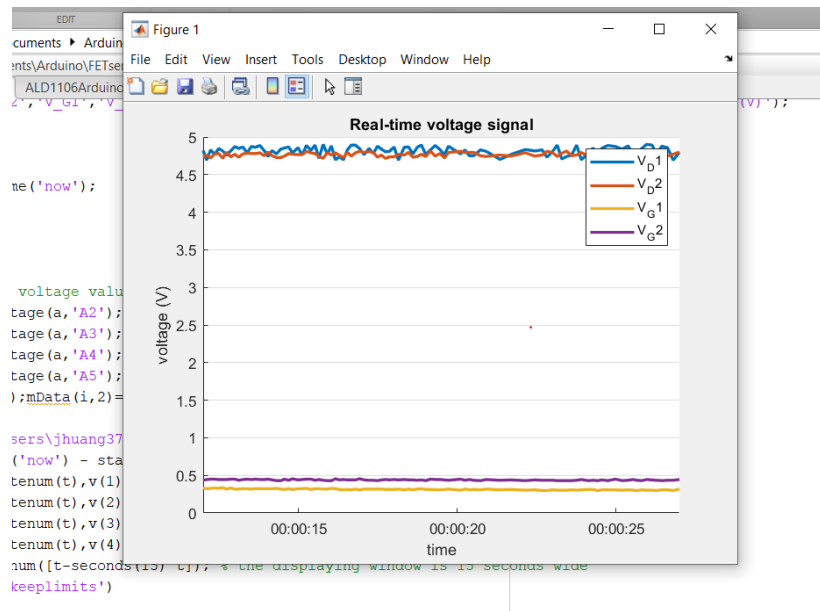


Figure A- 33. Screenshot of the MATLAB & Arduino Serial Communication

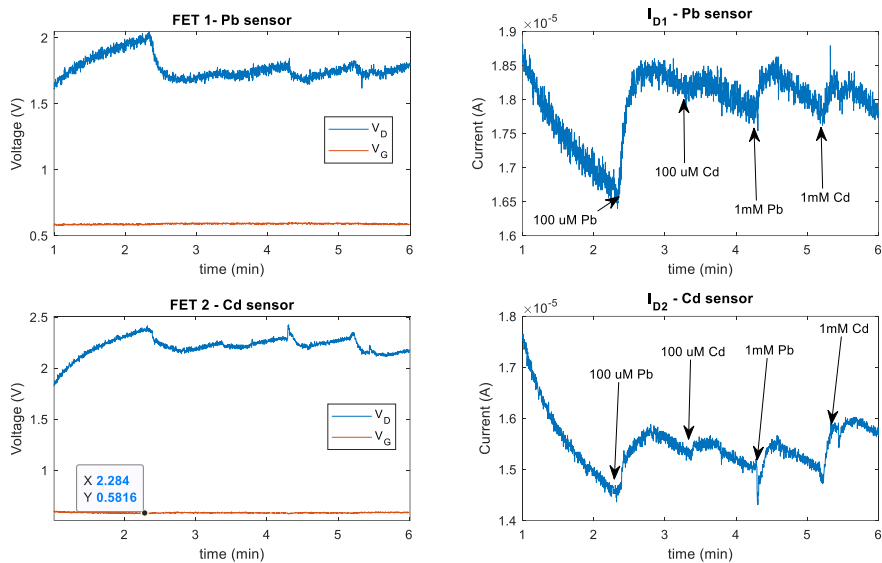


Figure A- 34. Potentiometric sensing result

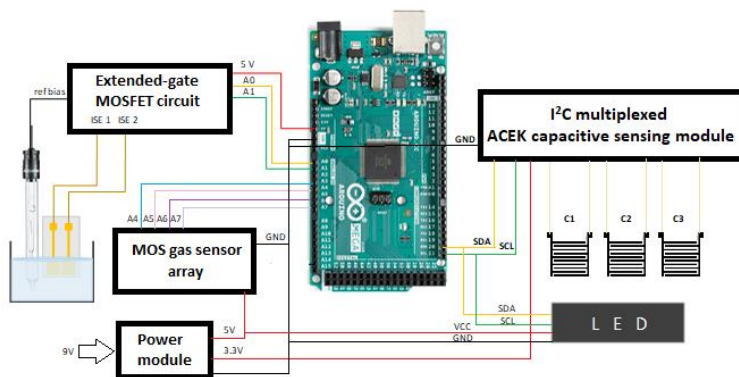


Figure A- 35. Schematic of the multi-mode sensing system

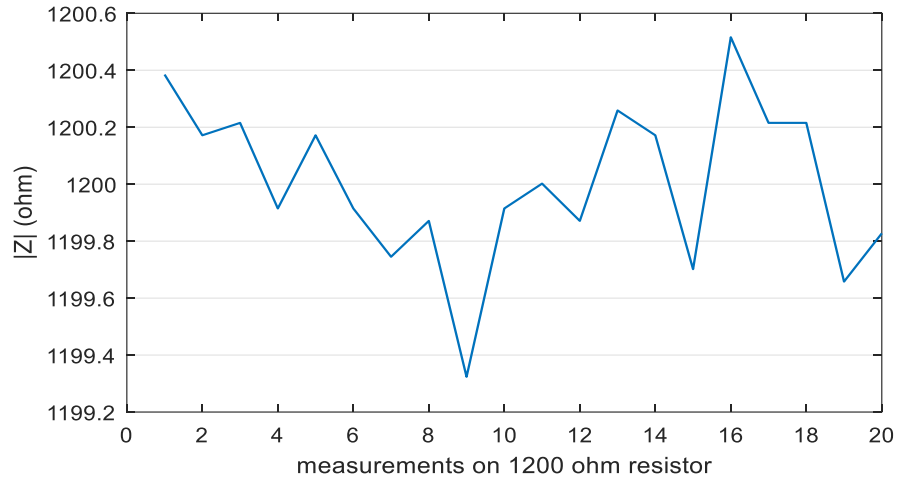


Figure A- 36. Calibration test with 1200Ω resistor

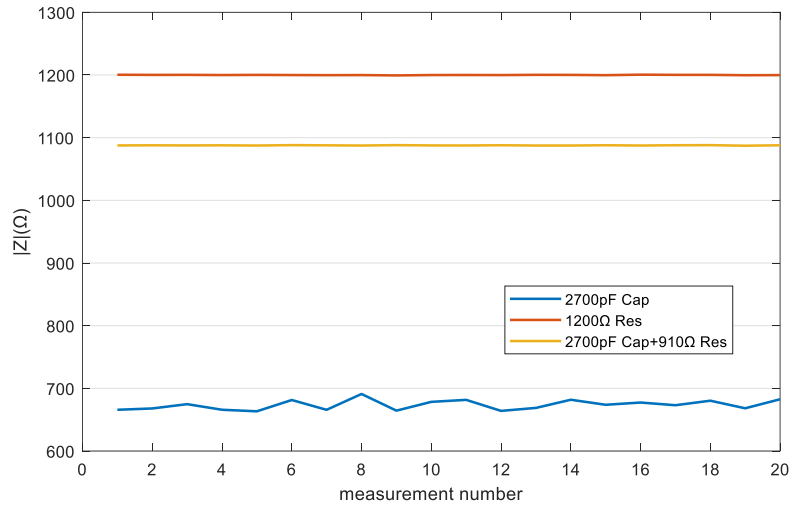


Figure A- 37. Impedance reading of 2700pF capacitor at 100kHz

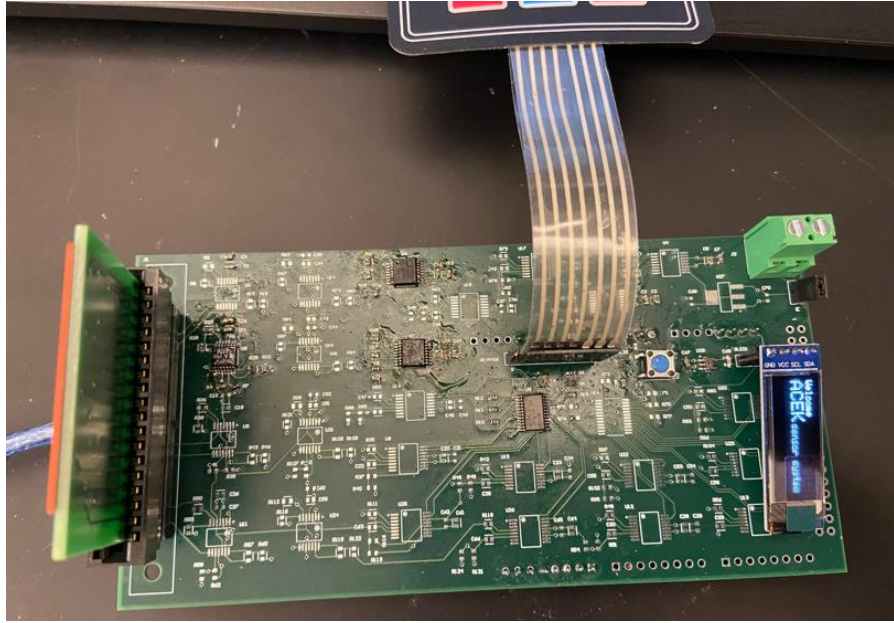


Figure A- 38. Photo of the ACEK impedance readout system

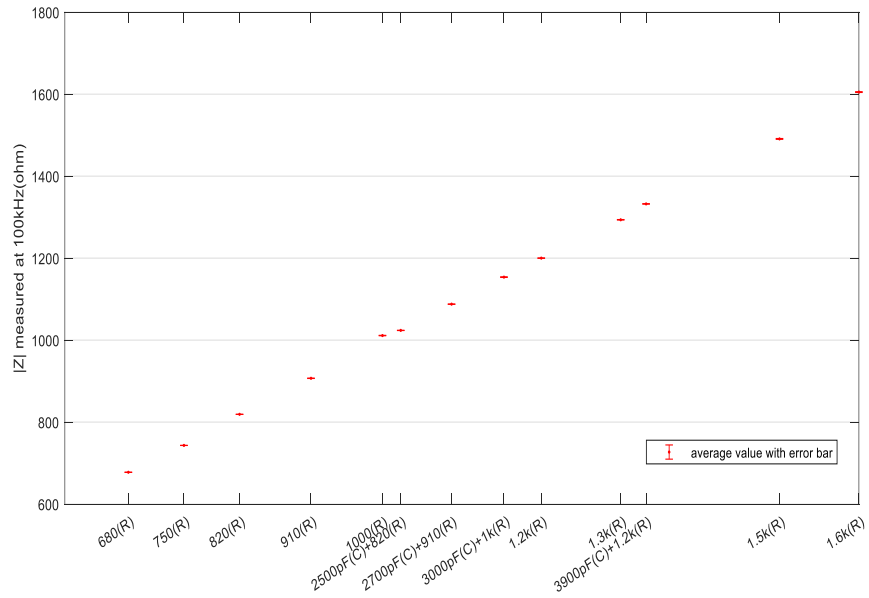
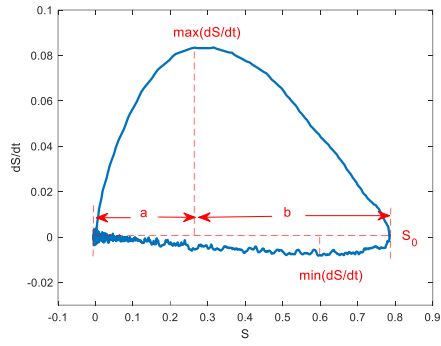
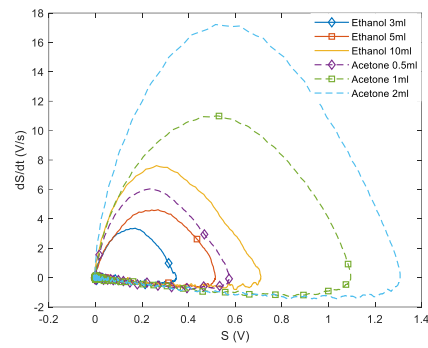


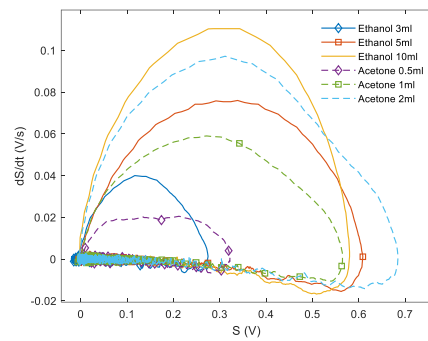
Figure A- 39. Impedance readings when calibrated with the 1200Ω resistor. Error bar shows the standard deviation.



(a)



(b)



(c)

Figure A- 40 (a) Response curve and parameters in phase space; Response curve to different amounts of ethanol and acetone in phase space, (b) TGS2602, (c) MQ136 (Solid line represents ethanol, dotted line represents acetone)

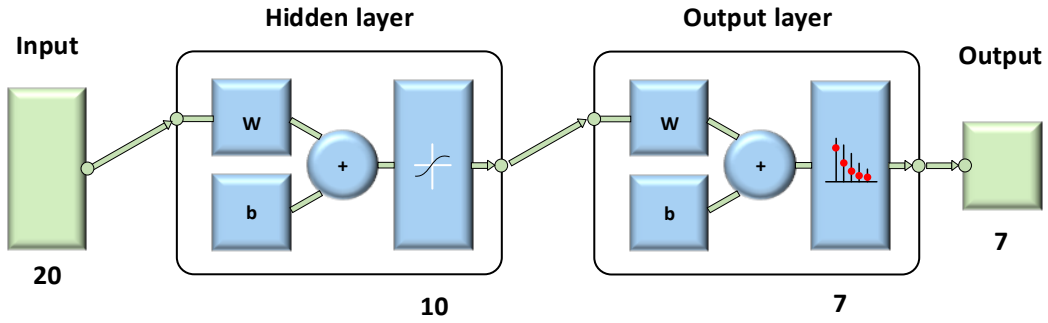
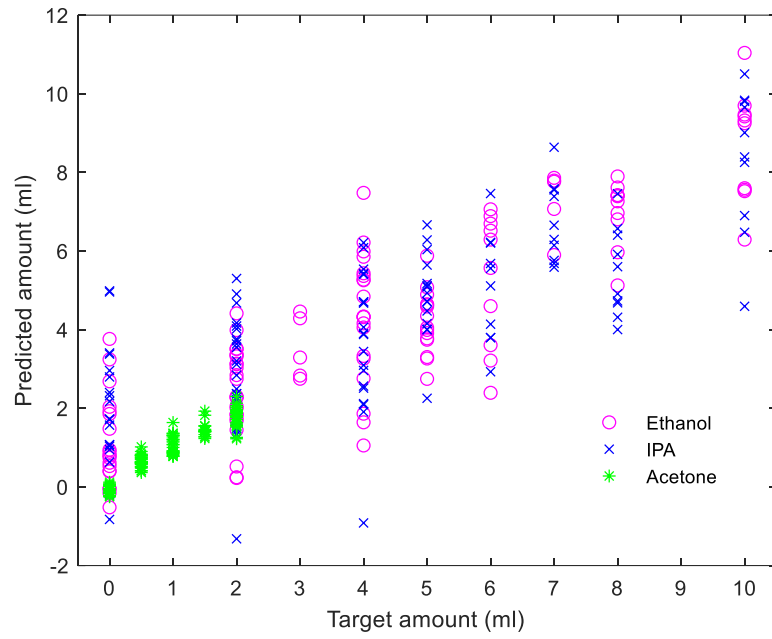


Figure A- 41. Diagram of the neural network

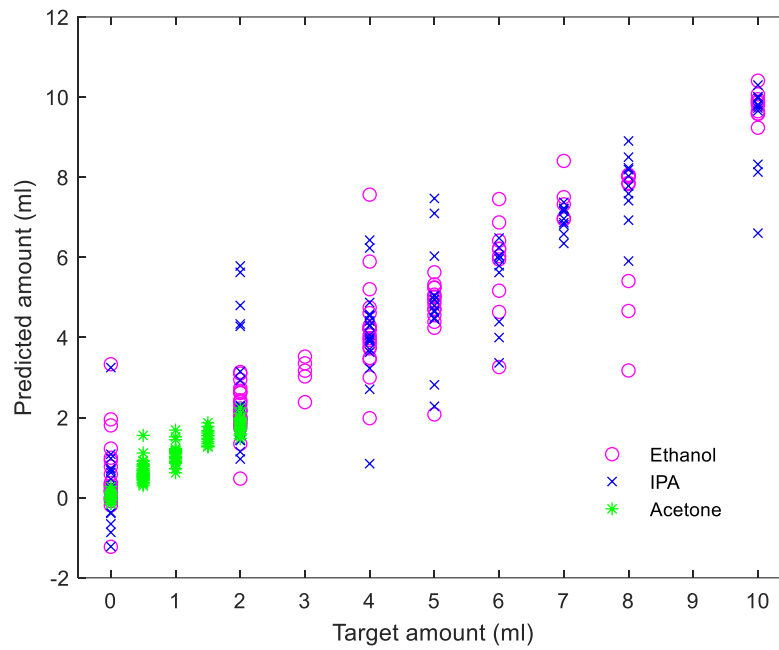
All Confusion Matrix

Output Class	1	14 9.3%	0 0.0%	0 0.0%	1 0.7%	1 0.7%	0 0.0%	0 0.0%	87.5%	12.5%
	2	0 0.0%	12 8.0%	0 0.0%	0 0.0%	0 0.0%	2 1.3%	0 0.0%	85.7%	14.3%
	3	0 0.0%	2 1.3%	15 10.0%	0 0.0%	0 0.0%	0 0.0%	0 0.0%	88.2%	11.8%
	4	1 0.7%	0 0.0%	0 0.0%	8 5.3%	1 0.7%	0 0.0%	2 1.3%	66.7%	33.3%
	5	0 0.0%	0 0.0%	0 0.0%	0 0.0%	10 6.7%	0 0.0%	2 1.3%	83.3%	16.7%
	6	0 0.0%	1 0.7%	0 0.0%	0 0.0%	0 0.0%	13 8.7%	0 0.0%	92.9%	7.1%
	7	0 0.0%	0 0.0%	0 0.0%	6 4.0%	3 2.0%	0 0.0%	56 37.3%	86.2%	13.8%
		93.3%	80.0%	100%	53.3%	66.7%	86.7%	93.3%	85.3%	6.7%
		6.7%	20.0%	0.0%	46.7%	33.3%	13.3%	6.7%	14.7%	
		1	2	3	4	5	6	7		
		Target Class								

Figure A- 42. Confusion matrix of classification results



(a)



(b)

Figure A- 43. Target versus predicted amount of gas in VOC mixture (a) Multivariate linear regression (b) BPNN

Table A- 1. Gas sensors in the array.

Sensor	Work condition	Sensitivity characteristic
MQ 135	$V_C, V_H: 5 \pm 0.1 \text{ V}; P_H \leq 800 \text{ mW}$	Rs: 30 k Ω ~200 k Ω (100ppm NH ₃) $\alpha \leq 0.65$ (200/50 NH ₃)
MQ 136	$V_C, V_H: 5 \pm 0.1 \text{ V}; P_H \leq 800 \text{ mW}$	Rs: 30 k Ω ~200 k Ω (10ppm H ₂ S) $\alpha \leq 0.65$ (20/5 H ₂ S)
TGS2600	$V_C, V_H: 5 \pm 0.2 \text{ V}; P_H: 210 \text{ mW}$	Rs: 10 k Ω ~90 k Ω (in air) $\beta = 0.3 \sim 0.6$ (10ppm H ₂ /air)
TGS2602	$V_C, V_H: 5 \pm 0.2 \text{ V}; P_H: 280 \text{ mW}$	Rs: 10 k Ω ~100 k Ω (in air) $\beta = 0.15 \sim 0.5$ (10ppm EtOH/air)
TGS2610	$V_C, V_H: 5 \pm 0.2 \text{ V}; P_H: 280 \text{ mW}$	Rs: 1 k Ω ~10 k Ω (in 1800ppm iso-butane) $\beta = 0.45 \sim 0.62$ (3000ppm/1000ppm iso-butane)
TGS2611	$V_C, V_H: 5 \pm 0.2 \text{ V}; P_H = 280 \pm 25 \text{ mW}$	Rs: 0.68 k Ω ~6.8 k Ω (in 5000ppm methane) $\beta = 0.60 \pm 0.06$ (9000ppm/3000ppm methane)

VC: circuit voltage; VH: heater voltage; PH: heater power consumption;
Rs: sensor resistance; α : concentration slope rate; β : change ratio of Rs.

Table A- 2. Correlation coefficient between sensors.

Sensor	MQ 135	MQ 136	TGS 2600	TGS 2602	TGS 2610	TGS2611
MQ 135	1	-	-	-	-	-
MQ 136	0.9499	1	-	-	-	-
TGS 2600	0.8363	0.9067	1	-	-	-
TGS 2602	0.7794	0.8321	0.9702	1	-	-
TGS 2610	0.9174	0.9855	0.9325	0.8447	1	-
TGS 2611	0.9408	0.9692	0.7998	0.6987	0.9409	1

Table A- 3. Principal component analysis of the sensor array.

PC	PC1	PC2	PC3	PC4	PC5	PC6
MQ 135	0.0193	0.0563	-0.1183	0.0855	-0.1215	0.9800
MQ 136	0.2510	0.7081	-0.4392	-0.2516	0.4228	-0.0243
TGS 2600	0.1441	0.0892	0.5017	-0.5653	0.6273	0.0810
TGS 2602	0.9332	-0.3415	-0.0739	-0.0302	-0.0776	-0.0147
TGS 2610	0.1997	0.5234	0.6608	-0.2286	-0.4441	0.0107
TGS 2611	0.0722	0.3113	-0.3152	0.7461	-0.4580	-0.1792
EXP	96.0152	3.8214	0.1293	0.0185	0.0116	0.0040

EXP: explained

VITA

Jiamei Huang attended Nanjing University of Aeronautics and Astronautics (Nanjing, China) in 2008 and received her B.S. and M.S. degrees in electrical engineering in June 2012 and March 2015. She worked at Pan Asia Technical Automotive Center (the research center of SAIC-GM, Shanghai, China) as electrical subsystem development and validation engineer from 2015 to 2017. She entered the University of Tennessee and became a graduate research assistant in spring 2019 and published two peer-reviewed journal articles as the first author in the following year.